



HAL
open science

On estimating the structure factor of a point process, with applications to hyperuniformity

Diala Hawat, Guillaume Gautier, Rémi Bardenet, Raphaël Lachièze-Rey

► **To cite this version:**

Diala Hawat, Guillaume Gautier, Rémi Bardenet, Raphaël Lachièze-Rey. On estimating the structure factor of a point process, with applications to hyperuniformity. 2022. hal-03615250v1

HAL Id: hal-03615250

<https://hal.science/hal-03615250v1>

Preprint submitted on 22 Jul 2022 (v1), last revised 27 Dec 2022 (v2)

HAL is a multi-disciplinary open access archive for the deposit and dissemination of scientific research documents, whether they are published or not. The documents may come from teaching and research institutions in France or abroad, or from public or private research centers.

L'archive ouverte pluridisciplinaire **HAL**, est destinée au dépôt et à la diffusion de documents scientifiques de niveau recherche, publiés ou non, émanant des établissements d'enseignement et de recherche français ou étrangers, des laboratoires publics ou privés.

On estimating the structure factor of a point process, with applications to hyperuniformity

Diala Hawat^{1,2*}, Guillaume Gautier¹, Rémi Bardenet¹
and Raphaël Lachièze-Rey²

¹Université de Lille, CNRS, Centrale Lille, UMR 9189 – CRISTAL
Lille, France.

² Université de Paris Cité, MAP5, Paris, France.

*Corresponding author(s). E-mail(s): diala.hawat@univ-lille.fr;

Abstract

Hyperuniformity is the study of stationary point processes with a sub-Poisson variance in a large window. In other words, counting the points of a hyperuniform point process that fall in a given large region yields a small-variance Monte Carlo estimation of the volume. Hyperuniform point processes have received a lot of attention in statistical physics, both for the investigation of natural organized structures and the synthesis of materials. Unfortunately, rigorously proving that a point process is hyperuniform is usually difficult. A common practice in statistical physics and chemistry is to use a few samples to estimate a spectral measure called the structure factor, and evaluating its decay around zero provides a diagnostic of hyperuniformity. Different applied fields use however different estimators, and important algorithmic choices proceed from each field's lore. This paper provides a systematic survey and derivation of the structure factor's known or otherwise natural estimators. We also leverage the consistency of these estimators to contribute an asymptotically valid statistical test of hyperuniformity, and benchmark all estimators and hyperuniformity diagnostics on a set of examples. In an effort to make investigations of the structure factor and hyperuniformity systematic and reproducible, we further provide a `Python` toolbox [structure_factor](#), containing all the estimators and tools that we discuss.

Keywords: Structure factor estimators. Multitapering methods. Multiscale debiasing. Hyperuniformity test. Python toolbox.

Contents

| | | |
|----------|--|-----------|
| 1 | Introduction | 3 |
| 2 | Point processes and their structure factor | 4 |
| 2.1 | Point processes and their correlation measures | 5 |
| 2.2 | The Fourier transform | 5 |
| 2.3 | The structure factor | 7 |
| 2.4 | Hyperuniformity | 7 |
| 2.5 | Empirical diagnostics of hyperuniformity | 8 |
| 2.6 | Benchmark point processes | 9 |
| 2.6.1 | The KLY process | 9 |
| 2.6.2 | The Ginibre ensemble | 10 |
| 2.6.3 | The homogeneous Poisson point process | 10 |
| 2.6.4 | The Thomas point process | 11 |
| 3 | Estimators of the structure factor | 11 |
| 3.1 | Assuming stationarity | 12 |
| 3.1.1 | The scattering intensity | 12 |
| 3.1.2 | Tapered variants of the scattering intensity | 15 |
| 3.1.3 | The multitapered estimator | 17 |
| 3.1.4 | On the choice of tapers | 17 |
| 3.2 | Assuming stationarity and isotropy | 18 |
| 3.2.1 | Bartlett’s isotropic estimator | 18 |
| 3.2.2 | Using Ogata’s quadrature | 20 |
| 3.2.3 | Using the quadrature of Baddour and Chouinard | 22 |
| 4 | Statistical hyperuniformity test | 23 |
| 4.1 | The coupled sum estimator | 23 |
| 4.2 | Hyperuniformity multiscale test | 24 |
| 5 | Demonstrating all estimators using our toolbox | 25 |
| 5.1 | Basic software objects | 25 |
| 5.2 | Demonstrating estimators that only assume stationarity | 25 |
| 5.3 | Demonstrating estimators that assume isotropy | 29 |
| 5.4 | Hyperuniformity diagnostics | 32 |
| 6 | A quantitative comparison of the estimators | 35 |
| 6.1 | A note on computational costs | 35 |
| 6.2 | Measuring the accuracy of the estimators near zero | 36 |
| 6.3 | Comparing variants of the scattering intensity | 37 |
| 6.4 | Comparing estimators that assume isotropy | 38 |
| A | Proof of Proposition 3 | 44 |
| B | Validity of Assumption (53) | 45 |

1 Introduction

Condensed matter physicists have observed that, for some random particle systems, the variance of the number of points in a large window scales slower than the volume of that window, a phenomenon called *hyperuniformity* (Torquato, 2018). This statistical property, in turn, implies desirable physical properties for materials (Torquato, 2018, Section 14). Outside physics, hyperuniform point processes have generated broad interest in statistics, machine learning, and probability. By definition, a hyperuniform point process leads to a fast-decaying Monte Carlo error when estimating volumes. This variance reduction property makes hyperuniformity a natural concept for many statistical applications. Projection determinantal point processes (DPPs), a particular class of hyperuniform point processes, have thus been proposed for Monte Carlo integration (Bardenet and Hardy, 2020, Belhadji, Bardenet, and Chainais, 2019, 2020a), subsampling stochastic gradients (Bardenet, Ghosh, and Lin, 2021), or feature selection (Belhadji, Bardenet, and Chainais, 2020b). In probability, hyperuniform point processes also appear across all fields. The Ginibre ensemble, arguably one of the most famous DPPs arising from random matrix theory (Anderson, Guionnet, and Zeitouni, 2009), is a typical example of hyperuniform point processes. In stochastic geometry, and beyond DPPs, hyperuniform point processes appear, e.g., in the zeros of Gaussian analytic functions (Hough, Krishnapur, Peres, and Virág, 2009), or matching constructions (Klatt, Last, and Yogeshwaran, 2020). Intriguingly, there is also empirical evidence that repeatedly applying an algorithm involving local repulsion of points to an initial point process leads to a hyperuniform point process (Klatt et al., 2019). Across all these scientific fields, there is a need for statistical diagnostics of hyperuniformity.

In theory, under mild assumptions, a point process in \mathbb{R}^d is hyperuniform if and only if its structure factor $S(\mathbf{k})$ decays to zero as $\|\mathbf{k}\|_2$ goes to zero (Coste, 2021). The structure factor is the Fourier transform of a measure that encodes the pairwise correlations of a point process, and the behavior in zero of the structure factor reflects long-range correlations in the original point process. Given a realization of a point process, the standard empirical diagnostic of hyperuniformity thus involves estimating and plotting the structure factor of the underlying point process (Klatt et al., 2019, Torquato, 2018). This graphical assessment is however not standardized and often not described in full reproducible detail in the literature, with implementation choices and statistical properties often part of each field’s folklore. There is also no standard software to estimate structure factors. In this paper, we contribute (i) a survey of existing estimators of the structure factor and their main properties, (ii) a new asymptotically valid statistical test of hyperuniformity, and (iii) a modular, open-source Python package¹ that implements all these estimators and the corresponding existent hyperuniformity diagnostics together with the new statistical test.

¹<https://github.com/For-a-few-DPPs-more/structure-factor>

In Section 2, we introduce hyperuniformity and the relevant background. In Section 3, we rederive two families of estimators of the structure factor. The first family assumes that the underlying point process is stationary, while the second further requires isotropy in addition. We also review existing hyperuniformity diagnostics and contribute the first asymptotic test of hyperuniformity in Section 4, using the seminal debiasing techniques of [Rhee and Glynn \(2015\)](#). All estimators and diagnostics are implemented in a companion Python toolbox `structure_factor`, which we illustrate in Section 5 on four point processes exhibiting behaviors such as repulsion, spatial independence, and clustering. In Section 6, we numerically compare the accuracy of the estimators. We conclude with a few research leads in Section 6.4.

Related work

The closest work to the survey part of our paper is the preprint of [Rajala, Olhede, and Murrell \(2020\)](#). They introduce important new estimators based on the idea of tapering in time series analysis ([Percival and Walden, 2020](#)), and investigate central limit theorems for their estimators. On our end, we limit ourselves to a survey – including the estimators of [Rajala et al. \(2020\)](#) – and simpler properties like asymptotic unbiasedness and its relation to implicit implementation choices in statistical physics papers. One reason for this is our motivation for the study of hyperuniformity: hyperuniform point processes are unlikely to satisfy the assumptions² behind the central limit theorems referenced by [Rajala et al. \(2020\)](#). Moreover, our survey includes a broader choice of estimators, including numerical quadratures of Hankel transforms, and a companion Python package. Overall, we believe that the survey part of our paper and the paper of [Rajala et al. \(2020\)](#) are complementary.

Notation

Throughout this paper, bold lowercase letters like \mathbf{x}, \mathbf{r} indicate vectors in \mathbb{R}^d , and the corresponding non-bold characters are scalars. In particular, $\mathbf{x} = (x_1, \dots, x_d)$. Whenever not confusing, we use the same letter in different fonts for a vector and its Euclidean norm, i.e., $r = \|\mathbf{r}\|_2$ and $k = \|\mathbf{k}\|_2$.

2 Point processes and their structure factor

Investigating the hyperuniformity of a point process commonly goes through the visual inspection of its *structure factor*, also known as the *scaled spectral density function*. In this section, we introduce the key definitions to understand that procedure. For a general reference on point processes, we refer to [Chiu, Stoyan, Kendall, and Mecke \(2013\)](#). For hyperuniformity and structure factors, we primarily refer to [Torquato \(2018\)](#) for readers with a physics background, and to [Coste \(2021\)](#) for readers with a mathematics background.

²E.g., Hypothesis (H4) of [Biscio and Waagepetersen \(2019\)](#), when the linear statistic is the number of points, contradicts hyperuniformity.

2.1 Point processes and their correlation measures

Loosely speaking, a point process is a random set of points, such that we can count the number of points falling in any observation window. More formally, let a *configuration* of \mathbb{R}^d be a locally finite set $\mathcal{X} \subset \mathbb{R}^d$, i.e., for any compact K of \mathbb{R}^d , the cardinality $\mathcal{X}(K)$ of $\mathcal{X} \cap K$ is finite. The family \mathcal{N} of configurations of \mathbb{R}^d is endowed by the σ -algebra generated by the mappings $\mathcal{X} \mapsto \mathcal{X}(K)$, for K compact. A *point process* is a random element of \mathcal{N} .

In this paper, we restrict ourselves to *stationary (or homogeneous)* point processes, i.e., the law of the point process \mathcal{X} is identical to that of $\mathcal{X} + \mathbf{y} \triangleq \{\mathbf{x} + \mathbf{y}; \mathbf{x} \in \mathcal{X}\}$, for all $\mathbf{y} \in \mathbb{R}^d$. In that case, the *intensity measure* $\rho^{(1)}$ of \mathcal{X} , defined by

$$\rho^{(1)}(A) = \mathbb{E}[\mathcal{X}(A)],$$

is proportional to the Lebesgue measure. We then write $\rho^{(1)}(d\mathbf{x}) = \rho d\mathbf{x}$, and $\rho \geq 0$ is called the *intensity* of \mathcal{X} .

Assessing pairwise correlations in a point process, and – as we shall see – hyperuniformity, usually goes through estimating the two-point correlation measure $\rho^{(2)}$ of \mathcal{X} . It is formally defined by

$$\mathbb{E} \left[\sum_{\substack{\neq \\ \mathbf{x}, \mathbf{y} \in \mathcal{X}}} f(\mathbf{x}, \mathbf{y}) \right] = \int_{\mathbb{R}^d \times \mathbb{R}^d} f(\mathbf{x}, \mathbf{y}) \rho^{(2)}(d\mathbf{x}, d\mathbf{y}),$$

for any nonnegative measurable bounded function f with compact support. If \mathcal{X} is stationary with intensity $\rho \geq 0$, the previous expression can be factorized in

$$\int_{\mathbb{R}^d \times \mathbb{R}^d} f(\mathbf{x} + \mathbf{y}, \mathbf{y}) \rho^2 g_2(d\mathbf{x}) d\mathbf{y}, \tag{1}$$

where g_2 is called the *pair correlation measure*.

Intuitively, $g_2(d\mathbf{x})$ is the probability that \mathcal{X} has a point at location $d\mathbf{x}$, given that \mathcal{X} already contains the origin. If in addition g_2 has a density g w.r.t. the Lebesgue measure, i.e., $g_2(d\mathbf{x}) = g(\mathbf{x})d\mathbf{x}$, then g is called the *pair correlation function* of \mathcal{X} . Informally, $g(\mathbf{r})$ counts the pairs $(\mathbf{x}, \mathbf{y}) \in \mathcal{X} \times \mathcal{X}$ such that $\mathbf{x} - \mathbf{y} = \mathbf{r} \in \mathbb{R}^d$. Finally, when \mathcal{X} is assumed both stationary and *isotropic*, i.e., the distribution of \mathcal{X} is both, translation- and rotation-invariant, then the pair correlation function g is radial. In that case, we abusively write $g(\mathbf{r}) = g(r)$, where $r = \|\mathbf{r}\|_2$.

2.2 The Fourier transform

The Fourier transform \mathcal{F} of an integrable function $f : \mathbb{R}^d \rightarrow \mathbb{C}$ is the square integrable function

$$\mathcal{F}(f)(\mathbf{k}) = \int_{\mathbb{R}^d} f(\mathbf{x}) e^{-i\langle \mathbf{k}, \mathbf{x} \rangle} d\mathbf{x},$$

where $\langle \mathbf{k}, \mathbf{x} \rangle$ is the dot product of the *wavevector* \mathbf{k} by \mathbf{x} . If f is furthermore a radial function, denoted abusively by $f(\mathbf{r}) = f(r)$, where $r = \|\mathbf{r}\|_2$, then the Fourier transform of f is the corresponding *symmetric Fourier transform* \mathcal{F}_s , namely

$$\mathcal{F}_s(f)(k) = \mathcal{F}(f)(\mathbf{k}) = (2\pi)^{d/2} \int_0^\infty r^{d/2} f(r) \frac{J_{d/2-1}(kr)}{k^{d/2-1}} dr, \quad (2)$$

where $k = \|\mathbf{k}\|_2$ is called a *wavenumber*, and J_ν is the Bessel function of the first kind of order ν (Osgood, 2014). If we further define the *Hankel transform* of order $\nu \geq -1/2$ as

$$\mathcal{H}_\nu(f)(k) = \int_0^\infty f(r) J_\nu(kr) r dr, \quad \text{for } k \geq 0, \quad (3)$$

then (2) rewrites as

$$\mathcal{F}_s(f)(k) = \frac{(2\pi)^{d/2}}{k^{d/2-1}} \mathcal{H}_{d/2-1}(\tilde{f})(k), \quad (4)$$

where $\tilde{f} : x \mapsto f(x)x^{d/2-1}$. Finally, note that the Fourier transform can be generalized to tempered distributions through duality (Coste, 2021, Appendix B).

We now introduce a function, the Fourier transform of which will be central in studying the properties of spectral estimators based on point processes. Let $W \subset \mathbb{R}^d$ be a convex set, later called *observation window*, and denote by $|W|$ its Lebesgue measure, i.e., its volume. The *scaled intersection volume* is the function

$$\alpha_0(\mathbf{r}, W) = \frac{1}{|W|} \int_{\mathbb{R}^d} \mathbf{1}_W(\mathbf{r} + \mathbf{y}) \mathbf{1}_W(\mathbf{y}) d\mathbf{y}, \quad (5)$$

and its Fourier transform is given by

$$\mathcal{F}(\alpha_0)(\mathbf{k}, W) = \frac{1}{|W|} (\mathcal{F}(\mathbf{1}_W)(\mathbf{k}))^2. \quad (6)$$

In particular, if $W = B^d(\mathbf{0}, R)$ is the Euclidean ball of radius R , the scaled intersection volume function (5) is radial (Torquato, 2018, Section 3.1.1). In this case, we abusively write $\alpha_0(\mathbf{r}, W) = \alpha_0(r, W)$ and

$$\mathcal{F}_s(\alpha_0)(k, W) = 2^d \pi^{d/2} \frac{\Gamma(1 + d/2)}{k^d} J_{d/2}^2(kR), \quad (7)$$

where Γ is Euler's Gamma function. On the other hand, if $W = \prod_{j=1}^d [-L_j/2, L_j/2]$, Equation (6) simplifies to

$$\mathcal{F}(\alpha_0)(\mathbf{k}, W) = \left(\prod_{j=1}^d \frac{\sin(k_j L_j/2)}{k_j \sqrt{L_j/2}} \right)^2. \tag{8}$$

2.3 The structure factor

The *structure factor measure* \mathcal{S} of a stationary point process \mathcal{X} in \mathbb{R}^d with intensity $\rho > 0$ is the measure on \mathbb{R}^d , when it exists, defined by

$$\mathcal{S} = \mathcal{L}^d + \rho \mathcal{F}[g_2 - \mathcal{L}^d] = \mathcal{F}(\delta_0 + \rho(g_2 - \mathcal{L}^d)), \tag{9}$$

where \mathcal{L}^d is the d -dimensional Lebesgue measure and δ_0 is the Dirac mass in 0. When the measure \mathcal{S} is absolutely continuous w.r.t. the Lebesgue measure, i.e., $\mathcal{S}(d\mathbf{k}) = S(\mathbf{k})d\mathbf{k}$, we call S the *structure factor*.³ When g_2 is absolutely continuous w.r.t. the Lebesgue measure and $g - 1$ is integrable, S can be explicitly written as

$$S(\mathbf{k}) = 1 + \rho \mathcal{F}(g - 1)(\mathbf{k}). \tag{10}$$

If \mathcal{X} is further assumed to be isotropic with intensity $\rho > 0$, then both the pair correlation function g and the structure factor S are radial functions. Abusively denoting $S(k) = S(\mathbf{k})$, Equation (10) reads

$$S(k) = 1 + \rho \mathcal{F}_s(g - 1)(k), \tag{11}$$

see [Torquato \(2018, Section 2\)](#), which can be expressed analytically using (4) as

$$S(k) = 1 + \rho \frac{(2\pi)^{d/2}}{k^{d/2-1}} \int_0^\infty (g(r) - 1) r^{d/2} J_{d/2-1}(kr) dr. \tag{12}$$

Finally, if the pair correlation function g exists and is smooth, then one can expect that

$$S(\mathbf{k}) \xrightarrow{\|\mathbf{k}\|_2 \rightarrow \infty} 1.$$

On the other hand, the behavior of S in zero measures the fluctuations of g around 1 at large scales $\|\mathbf{r}\|_2 \gg 1$, which can in turn help quantify properties like hyperuniformity.

2.4 Hyperuniformity

A point process \mathcal{X} of \mathbb{R}^d is often said to be *hyperuniform* (or *super-homogeneous*) if the variance of the number of points that fall in a Euclidean

³The literature is inconsistent as to whether the structure factor is the measure \mathcal{S} or its density S . We choose the density, which is also sometimes known as the *scaled spectral density function*.

ball scales slower than the volume of that ball, i.e.

$$\lim_{R \rightarrow \infty} \frac{\text{Var}[\mathcal{X}(B(\mathbf{0}, R))]}{|B(\mathbf{0}, R)|} = 0, \quad (13)$$

where Var stands for the variance. Some comments are in order. Although hyperuniformity *a priori* depends on the shape of the window, e.g., a ball in (13), mild technical assumptions allow considering any growing window (Coste, 2021, Section 2). Second, being hyperuniform is not a standard feature of point processes; a homogeneous Poisson process, for instance, is not hyperuniform, as the ratio in (13) is a positive constant. Third, the most general definition of hyperuniformity goes through the structure factor of a point process (9); under the mild assumption that $g_2 - 1$ is a signed measure it is equivalent to (13), see Coste (2021, Proposition 2.2). Moreover, Torquato (2018, Section 5.3.2) states that if the structure factor undergoes a power decay $|S(\mathbf{k})| \sim c\|\mathbf{k}\|_2^\alpha$ in the neighborhood of zero, the process can be classified into three categories depending on how α compares to 1, as summarized in Table 1.

Table 1: Classes of hyperuniformity

| Class | α | $\text{Var}[\mathcal{X}(B(\mathbf{0}, R))]$ |
|-------|--------------|---|
| I | > 1 | $\mathcal{O}(R^{d-1})$ |
| II | $= 1$ | $\mathcal{O}(R^{d-1} \log(R))$ |
| III | $\in]0, 1[$ | $\mathcal{O}(R^{d-\alpha})$ |

Since the variance cannot grow more slowly than R^{d-1} for a spherical window (Beck, 1987), Class I represents the *strongest* form of hyperuniformity. It includes, for instance, the Ginibre point process, as we shall see in Section 2.1. Class II hyperuniform processes include, for instance, the sine process, a central object in random matrix theory (Anderson et al., 2009). By contrast, systems that fall in Class III present the *weakest* form of hyperuniformity. Many stationary point processes are believed to be Class III, although few rigorous proofs exist; one can mention the asymptotic result of (Boursier, 2021) for the one-dimensional Riesz gaz.

2.5 Empirical diagnostics of hyperuniformity

As suggested in Section 2.4, the behavior in zero of the structure factor quantifies hyperuniformity. Investigating whether one or several samples come from a hyperuniform point process is thus often carried out by estimating the structure factor, and then either visually inspecting the resulting plots around zero, or regressing the estimated values. Say for a stationary and isotropic point process, one option is to regress $\log S$ onto $\log k$ around zero, to assert a potential value for the decay rate α in Table 1.

Another criterion of *effective* hyperuniformity has been proposed; see Klatt et al. (2019, Supplementary material) and Torquato (2018, Section 11.1.6). For

a stationary and isotropic hyperuniform point process, given a set of estimated values

$$\{(k_1, \widehat{S}(k_1)), \dots, (k_n, \widehat{S}(k_n))\}$$

with $k_1, \dots, k_n > 0$, the H -index is defined by

$$H = \frac{\widehat{S}(0)}{\widehat{S}(k_{\text{peak}})}, \quad (14)$$

where $\widehat{S}(0)$ is a linear extrapolation of the structure factor in $k = 0$ based on the estimated values of S , and k_{peak} is the location of the first dominant peak value of the estimated structure factor, defined here as

$$k_{\text{peak}} = \inf_i \{k_i; \widehat{S}(k_i) > 1, \widehat{S}(k_{i-1}) < \widehat{S}(k_i), \text{ and } \widehat{S}(k_{i+1}) < \widehat{S}(k_i)\},$$

and, say, k_{peak} defined arbitrarily in the unlikely case that the set is empty. When $H < 10^{-3}$, the process is called *effectively hyperuniform* by [Torquato \(2018, Section 11.1.6\)](#). Note that the linear extrapolation is chosen for simplicity and not based on model selection. Like the threshold of 10^{-3} , the definition of a dominant peak is also somewhat arbitrary. In [Section 4](#), we will introduce a novel statistical test that bypasses some of these arbitrary choices.

Finally, both an estimate of the decay rate from [Table 1](#) and the H -index [\(14\)](#) require estimators of the structure factor. Before we survey these estimators, we introduce a few benchmark point processes and discuss their structure factors.

2.6 Benchmark point processes

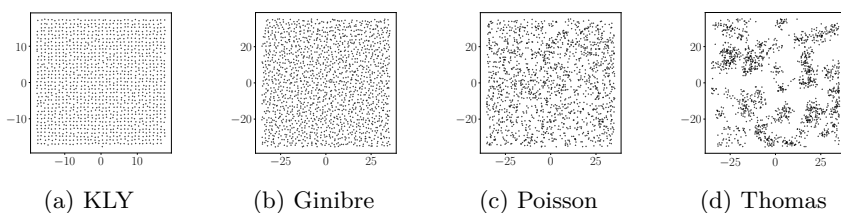


Fig. 1: A sample of each of our four benchmark point processes

2.6.1 The KLY process

Our first benchmark point process is the result of a matching algorithm proposed by [Klatt, Last, and Yogeshwaran \(2020\)](#). Loosely speaking, each point of \mathbb{Z}^d is matched with a close-by point of a user-defined point process in \mathbb{R}^d , like a homogeneous Poisson point process. The KLY process is an example of a

point process that is known to be stationary, ergodic, and hyperuniform (but not isotropic). However the corresponding pair correlation function, structure factor, and hyperuniformity class are unknown.

Klatt et al. (2020) use hyperuniformity diagnostics (Section 2.5) to assess the degree of hyperuniformity, and we shall reproduce their experiment with our software and all available estimators of the structure factor. Figure 1a shows a sample from the KLY process generated by matching a subset of \mathbb{Z}^2 with a realization of a Poisson point process with intensity $\rho = 11$. The intensity of the resulting point process is equal to 1. The same parameters are used to generate the samples from the KLY process used in Section 5.

2.6.2 The Ginibre ensemble

Our second hyperuniform point process is the Ginibre ensemble in $\mathbb{C} \approx \mathbb{R}^2$, both stationary and isotropic. The Ginibre ensemble can be defined (and approximately sampled) as the limit of the set of eigenvalues of matrices filled with i.i.d. standard complex Gaussian entries, as the size of the matrix goes to infinity (Hough et al., 2009, Theorem 4.3.10). A sample is shown in Figure 1b as well.

Its intensity is equal to $\rho_{\text{Ginibre}} = 1/\pi$, and its pair correlation function (Figure 2a) is

$$g_{\text{Ginibre}}(r) = 1 - \exp(-r^2). \quad (15)$$

The structure factor (Figure 2b) can be computed exactly,

$$S_{\text{Ginibre}}(k) = 1 - \exp(-k^2/4). \quad (16)$$

In particular, we have,

$$S_{\text{Ginibre}}(k) \sim k^2, \quad \text{for } k \rightarrow 0. \quad (17)$$

Thus, according to Table 1, the Ginibre ensemble is a hyperuniform point process of Class I, with $\alpha = 2$. Much is known about the Ginibre ensemble, and we use it to benchmark our toolbox and its different estimators, rather than to infer new results about it.

2.6.3 The homogeneous Poisson point process

The homogeneous Poisson point process of intensity ρ of \mathbb{R}^d is stationary and isotropic. It is often thought of as having as little structure as possible and can be defined as the limit of N uniform i.i.d. points in a window of volume N/ρ , as N goes to infinity. In particular, for any collection of mutually disjoint measurable subsets of \mathbb{R}^d , the number of points that fall in these subsets are independent; Figure 1c displays a realization from a Poisson process with the same intensity $\rho_{\text{Poisson}} = 1/\pi$ as the Ginibre ensemble. In the same vein, the pair correlation function and the structure factor of the Poisson point process are both equal to one; see Figures 2a and 2b. The Poisson process is not hyperuniform.

2.6.4 The Thomas point process

The Thomas point process is a point process in \mathbb{R}^d that is reminiscent of a mixture of Gaussians and typically exhibits clusters (Chiu et al., 2013, Section 5.3). Formally, consider a homogeneous Poisson point process $\mathcal{X}_{\text{parent}}$ of intensity ρ_{parent} , and let λ, σ be positive. Conditionally to $\mathcal{X}_{\text{parent}}$, let $(N_{\mathbf{x}})_{\mathbf{x} \in \mathcal{X}_{\text{parent}}}$ be i.i.d. Poisson variables with mean λ . For any $\mathbf{x} \in \mathcal{X}_{\text{parent}}$, conditionally to $N_{\mathbf{x}}$, let $(Y_{\mathbf{x},i})_{i=1}^{N_{\mathbf{x}}}$ be i.i.d. centered two-dimensional isotropic Gaussian vectors with variance σ . The resulting Thomas process is given by

$$\mathcal{X}_{\text{Thomas}} = \cup_{\mathbf{x} \in \mathcal{X}_{\text{parent}}} \{\mathbf{x} + Y_{\mathbf{x},i}, i = 1, \dots, N_{\mathbf{x}}\},$$

and its intensity is given by $\rho_{\text{Thomas}} = \rho_{\text{parent}} \times \lambda$. Figure 1d shows a realization of a Thomas point process of intensity $1/\pi$, generated from a parent Poisson point process of intensity $\rho_{\text{parent}} = 1/(20\pi)$, and a standard deviation $\sigma = 2$. Since σ is small enough compared to $\lambda = 20$, clusters naturally appear. The pair correlation function and the structure factor of the Thomas process, see Figures 2a and 2b, are both radial functions (Chiu et al., 2013, Equation 5.52), given by

$$g_{\text{Thomas}}(r) = 1 + \frac{1}{\rho_{\text{parent}} (\sqrt{4\pi\sigma^2})^d} \exp\left(-\frac{r^2}{4\sigma^2}\right), \quad (18)$$

and

$$S_{\text{Thomas}}(k) = 1 + \lambda \exp(-k^2\sigma^2). \quad (19)$$

The intuition that the Thomas point process is not hyperuniform is confirmed by the expression of the structure factor (19) which is even larger than 1.

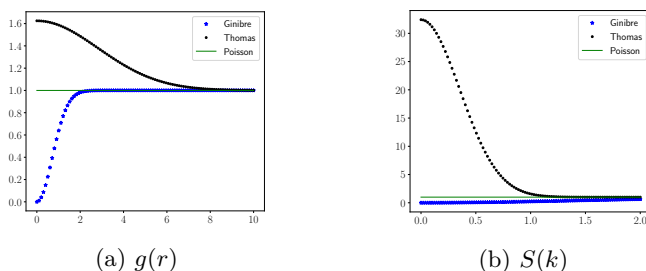


Fig. 2: Pair correlation functions $g(r)$ and structure factors $S(k)$ of some point processes

3 Estimators of the structure factor

Starting from the theoretical definition (10) of the structure factor, we derive all known estimators and add a few other natural candidates based on

numerical quadratures of the symmetric Fourier transform. We pay particular attention to the sources of asymptotic (in the size of the window) bias for each estimator. We split the estimators according to whether they only assume stationarity or stationarity *and* isotropy.

3.1 Assuming stationarity

The most common estimator of the structure factor is the so-called *scattering intensity* (Coste, 2021, Klatt et al., 2019, 2020, Torquato, 2018). Its name stems from its origins in the physics of diffraction, and it corresponds to a scaled version of Bartlett’s periodogram in time series analysis. After introducing the scattering intensity, we follow Rajala et al. (2020), who generalize it to so-called *tapered* estimators. We group our assumptions and notation in Assumption A1.

Assumption A1 \mathcal{X} is a stationary point process of \mathbb{R}^d with intensity $\rho > 0$. Its pair correlation function g exists, and $\mathbf{r} \mapsto g(\mathbf{r}) - 1$ is integrable on \mathbb{R}^d . Moreover, we only observe a realization of

$$\mathcal{X} \cap W = \{\mathbf{x}_1, \dots, \mathbf{x}_N\}$$

in a centered, rectangular window

$$W = \prod_{j=1}^d [-L_j/2, L_j/2].$$

We write $\mathbf{L} = (L_1, \dots, L_d)$.

3.1.1 The scattering intensity

In the physics literature, the following derivation is often assumed to be known to reader, and it seemed worthwhile to us to make it explicit. This allows, in particular, to understand the role played by the so-called *allowed wavevectors*. Note that Rajala et al. (2020) provide similar derivations.

The basic idea is to introduce the scaled intersection volume α_0 (5) in the definition (10) of the structure factor. We obtain

$$\begin{aligned} S(\mathbf{k}) &= 1 + \rho \int_{\mathbb{R}^d} (g(\mathbf{r}) - 1) e^{-i\langle \mathbf{k}, \mathbf{r} \rangle} \, d\mathbf{r} \\ &= 1 + \rho \int_{\mathbb{R}^d} \lim_{W \uparrow \mathbb{R}^d} (g(\mathbf{r}) - 1) \alpha_0(\mathbf{r}, W) e^{-i\langle \mathbf{k}, \mathbf{r} \rangle} \, d\mathbf{r} \\ &= 1 + \lim_{W \uparrow \mathbb{R}^d} \rho \int_{\mathbb{R}^d} (g(\mathbf{r}) - 1) \alpha_0(\mathbf{r}, W) e^{-i\langle \mathbf{k}, \mathbf{r} \rangle} \, d\mathbf{r}, \end{aligned} \quad (20)$$

where we used dominated convergence and the limit $\lim_{W \uparrow \mathbb{R}^d} \alpha_0(\mathbf{r}, W) = 1$. In the notation $W \uparrow \mathbb{R}^d$, the limit is taken so that the window progressively covers the whole space at roughly equal speed in all directions, i.e., $\min_j L_j \rightarrow \infty$ in

Assumption A1. Splitting the integral from (20) into two, we shall recognize an expectation under our censored point process $\mathcal{X} \cap W$ and a bias term,

$$S(\mathbf{k}) - 1 = \lim_{W \uparrow \mathbb{R}^d} \left[\frac{\rho}{|W|} \int_{\mathbb{R}^d} \int_{\mathbb{R}^d} \underbrace{e^{-i\langle \mathbf{k}, \mathbf{r} \rangle} \mathbb{1}_{W \times W}(\mathbf{r} + \mathbf{y}, \mathbf{y})}_{f(\mathbf{r} + \mathbf{y}, \mathbf{y})} g(\mathbf{r}) d\mathbf{y} d\mathbf{r} - \underbrace{\rho \mathcal{F}(\alpha_0)(\mathbf{k}, W)}_{\epsilon_0(\mathbf{k}, \mathbf{L})} \right].$$

Now, by definition (1) of the pair correlation measure, and still for any $\mathbf{k} \in \mathbb{R}^d$, $S(\mathbf{k}) - 1$ is the limit as $W \uparrow \mathbb{R}^d$ of

$$\frac{\rho}{\rho^2 |W|} \mathbb{E} \left[\sum_{\substack{\mathbf{x} \neq \mathbf{y} \\ \mathbf{x}, \mathbf{y} \in \mathcal{X}} \mathbb{1}_W(\mathbf{x}) \mathbb{1}_W(\mathbf{y}) e^{-i\langle \mathbf{k}, \mathbf{x} - \mathbf{y} \rangle} \right] - \epsilon_0(\mathbf{k}, \mathbf{L}),$$

so that

$$\begin{aligned} S(\mathbf{k}) &= \lim_{W \uparrow \mathbb{R}^d} \frac{1}{\rho |W|} \mathbb{E} \left[\sum_{\mathbf{x}, \mathbf{y} \in \mathcal{X} \cap W} e^{-i\langle \mathbf{k}, \mathbf{x} - \mathbf{y} \rangle} \right] - \epsilon_0(\mathbf{k}, \mathbf{L}) \\ &= \lim_{W \uparrow \mathbb{R}^d} \frac{1}{\rho |W|} \mathbb{E} \left[\left| \sum_{\mathbf{x} \in \mathcal{X} \cap W} e^{-i\langle \mathbf{k}, \mathbf{x} \rangle} \right|^2 \right] - \epsilon_0(\mathbf{k}, \mathbf{L}). \end{aligned} \quad (21)$$

Note that, by (8), the bias term satisfies

$$\begin{aligned} |\epsilon_0(\mathbf{k}, \mathbf{L})| &= \rho \frac{\mathcal{F}^2(\mathbb{1}_W)(\mathbf{k})}{|W|} = \rho \left(\prod_{j=1}^d \frac{\sin(k_j L_j / 2)}{\sqrt{L_j k_j / 2}} \right)^2 \\ &\leq \begin{cases} 0 & \text{if } \mathbf{k} \in \mathbb{A}_{\mathbf{L}}, \\ \rho \prod_{j=1}^d L_j & \text{as } \|\mathbf{k}\|_2 \rightarrow 0, \\ 2^{2d} \prod_{j=1}^d \frac{1}{L_j k_j^2} & \text{as } \|\mathbf{k}\|_2 \rightarrow \infty, \end{cases} \end{aligned}$$

where we defined

$$\mathbb{A}_{\mathbf{L}} = \left\{ \mathbf{k} \in (\mathbb{R}^*)^d \text{ s.t. } k_j = \frac{2\pi n}{L_j} \text{ for some } j \in \{1, \dots, d\} \text{ and } n \in \mathbb{Z}^* \right\}. \quad (22)$$

We have thus proved the following proposition.

Proposition 1 *Under Assumption A1, for $\mathbf{k} \in \mathbb{A}_{\mathbf{L}}$, the scattering intensity estimator*

$$\widehat{S}_{\text{SI}}(\mathbf{k}) \triangleq \frac{1}{\rho |W|} \left| \sum_{j=1}^N e^{-i\langle \mathbf{k}, \mathbf{x}_j \rangle} \right|^2 \quad (23)$$

is asymptotically unbiased, i.e.,

$$\sup_{\mathbf{k} \in \mathbb{A}_{\mathbf{L}}} \left| \mathbb{E}[\widehat{S}_{\text{SI}}(\mathbf{k})] - S(\mathbf{k}) \right| \xrightarrow{W \uparrow \mathbb{R}^d} 0.$$

This motivates restricting to $\mathbf{k} \in \mathbb{A}_{\mathbf{L}}$ if one is interested in estimating the behavior of S in zero. In the literature, the scattering intensity is actually often evaluated on a subset of $\mathbb{A}_{\mathbf{L}}$, namely

$$\mathbb{A}_{\mathbf{L}}^{\text{res}} = \left\{ \left(\frac{2\pi n_1}{L_1}, \dots, \frac{2\pi n_d}{L_d} \right); \mathbf{n} \in (\mathbb{Z}^*)^d \right\}. \quad (24)$$

The set $\mathbb{A}_{\mathbf{L}}^{\text{res}}$ is called the set of *allowed wavevectors* in physics (Klatt et al., 2020, Section 10), or part of the *dual lattice* of fundamental cell W in sampling theory (Osgood, 2014, Chapter 5), or *Fourier grid* in time series analysis (Rajala et al., 2020). We add the superscript *res* to underline that it is actually a restriction of the set $\mathbb{A}_{\mathbf{L}}$ of wavevectors justified by the cancellation of the asymptotic bias.

It is unclear to us why one should consider $\mathbb{A}_{\mathbf{L}}^{\text{res}}$ instead of $\mathbb{A}_{\mathbf{L}}$. In particular, the minimal *wavenumber* (the norm of a wavevector) in $\mathbb{A}_{\mathbf{L}}^{\text{res}}$ is

$$k_{\min}^{\text{res}} = 2\pi \sqrt{\sum_{j=1}^d L_j^{-2}},$$

while working with $\mathbb{A}_{\mathbf{L}}$ in (22) relaxes this threshold to a k_{\min} satisfying

$$\frac{2\pi}{\max_j L_j} < k_{\min} < k_{\min}^{\text{res}}.$$

To see how far we can hope going down in $k > 0$, we give evidence below as to why the scattering intensity should never be evaluated for $\|\mathbf{k}\|_2 \leq \frac{\pi}{\sqrt{d} \max_j L_j}$.

Finally, when ρ is unknown, and \mathcal{X} is further assumed to be ergodic, it is common to replace the denominator $\rho|W|$ by N in (23), leading to the self-normalized scattering intensity estimator

$$\widehat{S}_{\text{SI},s}(\mathbf{k}) \triangleq \frac{1}{N} \left| \sum_{j=1}^N e^{-i\langle \mathbf{k}, \mathbf{x}_j \rangle} \right|^2. \quad (25)$$

Indeed, by ergodicity,

$$\frac{\widehat{S}_{\text{SI},s}}{\widehat{S}_{\text{SI}}} \xrightarrow{W \uparrow \mathbb{R}^d} 1 \text{ a.s.}$$

Many authors define the scattering intensity as its self-normalized version (Coste, 2021, Klatt et al., 2019, Torquato, 2018), but we argue that when ρ is known, it is not clear whether this estimator has a smaller mean squared

error than (23). For the reader interested in second order properties of this estimator, its second moment on Poisson input is derived in Appendix B.

A lower bound for k_{\min} .

It is clear that when W is fixed, the scattering intensity (25) is not relevant when \mathbf{k} is too close to 0, since for a fixed sample $\mathcal{X}_N = \{\mathbf{x}_1, \dots, \mathbf{x}_N\}$,

$$\lim_{\mathbf{k} \rightarrow 0} \widehat{S}_{\text{SI},s}(\mathbf{k}) = N.$$

The theoretical convergence to 0 for hyperuniform processes is dictated by the compensation occurring between exponential terms $e^{-i\langle \mathbf{k}, \mathbf{x}_j \rangle}$ on large portions of the space. One can safely infer that if a large portion of the terms gives a positive contribution, then the compensation does not occur and the global result will not be accurate. Still with the notation in Assumption A1, if $\|\mathbf{k}\|_2 < \frac{\pi}{\sqrt{d} \max_j L_j}$, then for $\mathbf{x} \in W$, $|\langle \mathbf{x}, \mathbf{k} \rangle| \leq \pi/2$, so that there exists $\epsilon > 0$ such that

$$\frac{1}{N} \left| \sum_{j=1}^N e^{-i\langle \mathbf{k}, \mathbf{x}_j \rangle} \right|^2 \geq \frac{(N\epsilon)^2}{N}.$$

Thus for any $\|\mathbf{k}\|_2 < \frac{\pi}{\sqrt{d} \max_j L_j}$, we have a lower bound of $\widehat{S}_{\text{SI},s}(\mathbf{k})$ that is independent of the point process, and which diverges as the number of points goes to infinity. Consequently, we argue that $\pi/\sqrt{d} \max_j L_j$ is a lower bound for accessible wavenumbers, which one might improve with a finer study of the estimator bias.

3.1.2 Tapered variants of the scattering intensity

The derivation of the scattering intensity can be generalized to the *tapered estimator*

$$\widehat{S}_{\text{T}}(t, \mathbf{k}) \triangleq \frac{1}{\rho} \left| \sum_{j=1}^N t(\mathbf{x}_j, W) e^{-i\langle \mathbf{k}, \mathbf{x}_j \rangle} \right|^2, \quad \mathbf{k} \in \mathbb{R}^d, \quad (26)$$

where $t(\cdot, W)$ is a uniformly (in W) square-integrable function supported on the observation window W , called a *taper*. The tapered estimator (26) corresponds to a scaled version of what is called a tapered periodogram in the signal processing literature (Rajala et al., 2020, Section 3). The vocabulary is adapted from the spectral analysis of time series, where tapers are now well established (Percival and Walden, 2020).

In particular, one recovers the scattering intensity (25) from the tapered formulation (26) by plugging the taper

$$t_0(\mathbf{x}, W) \triangleq \frac{1}{\sqrt{|W|}} \mathbf{1}_W(\mathbf{x}). \quad (27)$$

To follow the derivation of (21), we further let

$$\alpha_t(\mathbf{r}, W) \triangleq \int_{\mathbb{R}^d} t(\mathbf{r} + \mathbf{y}, W)t(\mathbf{y}, W)d\mathbf{y}, \quad (28)$$

and require that

$$\lim_{W \uparrow \mathbb{R}^d} \alpha_t(\mathbf{r}, W) = 1 \quad \text{and} \quad \alpha_t(\mathbf{0}, W) = 1, \quad (29)$$

where the limit is again taken as $\min_j L_j \rightarrow \infty$ under Assumption A1. Note first that our requirement that (29) holds differs from the treatment of Rajala et al. (2020). We find (29) to be a more natural generalization of the scattering intensity arguments of Torquato (2018). Note also that, for simplicity, we denoted α_{t_0} by α_0 in Section 2.2, and we shall stick to this simplified notation.

Now, Cauchy-Schwarz and the uniform integrability of t guarantee that $\alpha_t(\cdot, W)$ is uniformly (in W) bounded, so that by dominated convergence,

$$S(\mathbf{k}) = 1 + \rho \lim_{W \uparrow \mathbb{R}^d} \int_{\mathbb{R}^d} (g(\mathbf{r}) - 1)\alpha_t(\mathbf{r}, W)e^{-i\langle \mathbf{k}, \mathbf{r} \rangle} d\mathbf{r}.$$

Following the lines of (21), we obtain

$$S(\mathbf{k}) = \lim_{W \uparrow \mathbb{R}^d} \left(\mathbb{E} \left[\widehat{S}_T(t, \mathbf{k}) \right] - \underbrace{\rho |\mathcal{F}(t)(\mathbf{k}, W)|^2}_{\epsilon_t(\mathbf{k}, \mathbf{L})} \right). \quad (30)$$

where the tapered estimator \widehat{S}_T is defined in (26). To eliminate the asymptotic bias $\epsilon_t(\mathbf{k}, \mathbf{L})$, one can restrict oneself again to a set of allowed wavevectors as we did in (22), i.e., the zeros of $\epsilon_t(\cdot, \mathbf{L})$. For general tapers, however, finding these zeros is not straightforward, and an alternative way to escape the bias is to correct it, as in

$$\widehat{S}_{\text{UDT}}(t, \mathbf{k}) \triangleq \frac{1}{\rho} \left| \sum_{j=1}^N t(\mathbf{x}_j, W)e^{-i\langle \mathbf{k}, \mathbf{x}_j \rangle} \right|^2 - \rho |\mathcal{F}(t)(\mathbf{k}, W)|^2. \quad (31)$$

We refer to \widehat{S}_{UDT} as the *undirectly debiased tapered estimator*, which is a scaled version of what Rajala et al. (2020) define. The major issue of Estimator (31) is that it may give negative values. To remedy this, Rajala et al. (2020) propose to remove the bias inside the summation before taking the squared modulus, namely, to define the *directly debiased tapered estimator*

$$\widehat{S}_{\text{DDT}}(t, \mathbf{k}) \triangleq \frac{1}{\rho} \left| \sum_{j=1}^N t(\mathbf{x}_j, W)e^{-i\langle \mathbf{k}, \mathbf{x}_j \rangle} - \rho \mathcal{F}(t)(\mathbf{k}, W) \right|^2. \quad (32)$$

Finally, note that these debiasing techniques naturally apply to the special case of the scattering intensity, and thus offer an alternative to using allowed values (22).

3.1.3 The multitapered estimator

In the spectral analysis of time series, *multitapering* (MT) was first introduced by Thomson (1982); see also Percival and Walden (2020) for a modern reference. The idea is to average a periodogram over many tapers, in the hope to reduce the variance of the resulting estimator. Rajala et al. (2020) propose to adapt the method to point processes, and we follow their lines.

For any $\mathbf{k} \in \mathbb{R}^d$ and $P \in \mathbb{N}^*$, and under Assumption A1, Rajala et al. (2020) define the *multitapered estimator* \widehat{S}_{MT} by

$$\widehat{S}_{\text{MT}}((t_q)_{q=1}^P, \mathbf{k}) = \frac{1}{P} \sum_{q=1}^P \widehat{S}(t_q, \mathbf{k}), \quad (33)$$

where the P tapers $(t_q)_{q=1}^P$ are typically taken to be pairwise orthogonal square integrable functions, and $\widehat{S}(t_q, \cdot)$ is any of the tapered estimators, whether unbiased (26), undirectly debiased (31), or directly debiased (32). The directly and undirectly debiased versions of \widehat{S}_{MT} will be respectively denoted by $\widehat{S}_{\text{DDMT}}$ and $\widehat{S}_{\text{UDMT}}$.

3.1.4 On the choice of tapers

Common taper choices in time series analysis are Slepian tapers, sinusoidal tapers, and minimum bias tapers (Riedel and Sidorenko, 1995). For instance, still assuming a centered rectangular window $W = \prod_{j=1}^d [-L_j/2, L_j/2]$, the family of sinusoidal tapers $(t_q)_{q \geq 1}$ supported on W is defined by

$$t_q(\mathbf{x}, W) = t(\mathbf{x}, \mathbf{p}^q, W) \triangleq \frac{\mathbb{1}_W(\mathbf{x})}{\sqrt{|W|}} \prod_{j=1}^d \sqrt{2} \sin \left(\frac{\pi p_j^q}{L_j} \left(x_j + \frac{L_j}{2} \right) \right), \quad (34)$$

where $\mathbf{p}^q = (p_1^q, \dots, p_d^q) \in (\mathbb{N}^d)^*$ and $\mathbf{x} = (x_1, \dots, x_d) \in \mathbb{R}^d$. The sinusoidal tapers are pairwise orthogonal, and an easy direct computation shows that they also satisfy (29). Moreover, for $\mathbf{k} = (k_1, \dots, k_d) \in \mathbb{R}^d$ the Fourier transform $\mathcal{F}(t_q)(\mathbf{k}, W)$ of t_q for any q is

$$\frac{1}{\sqrt{|W|}} \prod_{j=1}^d \sqrt{2} i^{(p_j^q+1)} \left[\frac{\sin \left(\left(k_j - \frac{\pi p_j^q}{L_j} \right) \frac{L_j}{2} \right)}{k_j - \frac{\pi p_j^q}{L_j}} - (-1)^{p_j^q} \frac{\sin \left(\left(k_j + \frac{\pi p_j^q}{L_j} \right) \frac{L_j}{2} \right)}{k_j + \frac{\pi p_j^q}{L_j}} \right].$$

This closed-form expression can thus be used in any debiasing scheme.

3.2 Assuming stationarity and isotropy

For isotropic point processes, a common approach is simply to numerically rotation-average the structure factor estimators presented in Section 3.1. Alternatively, one could start from the analytical expression (11) of the structure factor as symmetric Fourier transform – a univariate integral – involving the pair correlation function. Then again, two approaches have been identified. First, identifying an expectation under the point process as in Section 3.1 leads to a natural estimator originally derived by Bartlett (1964). Second, estimation of the pair correlation followed by numerical quadrature leads to at least two natural estimators, depending on whether the quadrature is that of Ogata (2005), or that of Baddour and Chouinard (2015). We review all these estimators in turn. All point processes in Section 3.2 satisfy Assumption A2.

Assumption A2 \mathcal{X} is a stationary isotropic point process of \mathbb{R}^d , of intensity ρ . Its pair correlation function g exists, and $r \mapsto g(r) - 1$ is integrable. Moreover, we only observe a realization of $\mathcal{X} \cap W = \{\mathbf{x}_1, \dots, \mathbf{x}_N\}$ in the centered ball $W = B^d(\mathbf{0}, R)$.

3.2.1 Bartlett's isotropic estimator

From the observation that the scaled intersection volume α_0 (5) is a radial function, $\alpha_0(\mathbf{r}, W) = \alpha_0(r, W)$, and following the lines of Section 3.1, dominated convergence yields

$$S(k) - 1 = \lim_{R \rightarrow \infty} \left[\rho \frac{(2\pi)^{\frac{d}{2}}}{k^{\frac{d}{2}-1}} \int_0^\infty \alpha_0(r, W) g(r) r^{\frac{d}{2}} J_{d/2-1}(kr) dr - \underbrace{\rho \mathcal{F}(\alpha_0)(k, W)}_{\triangleq \epsilon_1(k, R)} \right]. \quad (35)$$

Now, precisely because α_0 is radial, we have

$$\alpha_0(r, W) = \frac{1}{\omega_{d-1}} \int_{S^{d-1}} \alpha_0(r\mathbf{u}, W) d\mathbf{u}, \quad (36)$$

where $d\mathbf{u}$ is the $(d-1)$ -dimensional Hausdorff measure and S^{d-1} is the unit sphere of \mathbb{R}^d , with surface area ω_{d-1} . Plugging (36) into (35) yields

$$\begin{aligned} S(k) - 1 &= \lim_{R \rightarrow \infty} \frac{\rho(2\pi)^{\frac{d}{2}} k^{1-\frac{d}{2}}}{|W|\omega_{d-1}} \int_{\mathbb{R}^+ \times S^{d-1} \times \mathbb{R}^d} \left(r^{\frac{d}{2}} J_{d/2-1}(kr) g(r) \right. \\ &\quad \left. \mathbf{1}_{W \times W}(r\mathbf{u} + \mathbf{y}, \mathbf{y}) \right) dy d\mathbf{u} dr - \epsilon_1(k, R) \\ &= \lim_{R \rightarrow \infty} \frac{\rho(2\pi)^{\frac{d}{2}}}{|W|\omega_{d-1}} \int_{\mathbb{R}^+ \times S^{d-1} \times \mathbb{R}^d} \left(\frac{J_{d/2-1}(kr)}{(kr)^{d/2-1}} g(r) \right) \end{aligned}$$

$$\begin{aligned}
 & \mathbb{1}_{W \times W}(\mathbf{r}\mathbf{u} + \mathbf{y}, \mathbf{y}) \Big) \, \mathrm{d}\mathbf{y}\mathrm{d}\mathbf{u} \, r^{d-1}\mathrm{d}r - \epsilon_1(k, R) \\
 = & \lim_{R \rightarrow \infty} \frac{\rho(2\pi)^{\frac{d}{2}}}{|W|\omega_{d-1}} \int_{\mathbb{R}^d \times \mathbb{R}^d} \mathbb{1}_{W \times W}(\mathbf{r} + \mathbf{y}, \mathbf{y}) \frac{J_{d/2-1}(k\|\mathbf{r}\|_2)}{(k\|\mathbf{r}\|_2)^{\frac{d}{2}-1}} g(\|\mathbf{r}\|_2) \, \mathrm{d}\mathbf{y}\mathrm{d}\mathbf{r} - \epsilon_1(k, R).
 \end{aligned}$$

We now recognize an expectation using (1), so that $S(k) - 1$ rewrites as

$$\lim_{R \rightarrow \infty} \frac{(2\pi)^{\frac{d}{2}}}{\rho|W|\omega_{d-1}} \mathbb{E} \left[\sum_{\substack{\mathbf{x} \neq \mathbf{y} \\ \mathbf{x}, \mathbf{y} \in \mathcal{X} \cap W}} \frac{J_{d/2-1}(k\|\mathbf{x} - \mathbf{y}\|_2)}{(k\|\mathbf{x} - \mathbf{y}\|_2)^{d/2-1}} \right] - \epsilon_1(k, R). \quad (37)$$

We thus define a new estimator

$$\widehat{S}_{\text{BI}}(k) = 1 + \frac{(2\pi)^{\frac{d}{2}}}{\rho|W|\omega_{d-1}} \sum_{\substack{i, j=1 \\ i \neq j}}^N \frac{J_{d/2-1}(k\|\mathbf{x}_i - \mathbf{x}_j\|_2)}{(k\|\mathbf{x}_i - \mathbf{x}_j\|_2)^{d/2-1}}, \quad (38)$$

along with its self-normalized version

$$\widehat{S}_{\text{BI},s}(k) = 1 + \frac{(2\pi)^{\frac{d}{2}}}{N\omega_{d-1}} \sum_{\substack{i, j=1 \\ i \neq j}}^N \frac{J_{d/2-1}(k\|\mathbf{x}_i - \mathbf{x}_j\|_2)}{(k\|\mathbf{x}_i - \mathbf{x}_j\|_2)^{d/2-1}}, \quad (39)$$

as in the case of the self-normalized scattering intensity (25). When $d = 2$, $\widehat{S}_{\text{BI},s}$ corresponds to Bartlett's isotropic estimator (Bartlett, 1964).

Here also, there are two sources of bias in the estimator (38). The first one is due to the restriction of the point process to a bounded observation window, which shall disappear as the window grows. The second source of bias $\epsilon_1(k, R)$ is again related to the Fourier transform of the scaled intersection volume $\alpha_0(\cdot, W)$. Diggle et al. (1987) observed that $|\epsilon_1(k, R)|$ is larger when $k > 0$ is small, and proposed to artificially set the value of the estimator to some constant when k is smaller than a certain threshold (Diggle et al., 1987, Equation 3.4). Obviously, this correction is inadequate to study hyperuniformity, i.e., the behavior of S near zero.

An alternative to Diggle's clipping procedure is to proceed as done for the scattering intensity (23) and estimate the structure factor only at a set of allowed wavenumbers, defined as the zeros of $\epsilon_1(\cdot, R)$. Using (7), it comes, for fixed d ,

$$\begin{aligned}
 \epsilon_1(k, R) &= \mathcal{F}(\alpha_0)(k) = 2^d \pi^{d/2} \frac{\Gamma(d/2 + 1)}{k^d} J_{\frac{d}{2}}^2(kR) \\
 &= \begin{cases} 0 & \text{if } k \in \{\frac{\pi}{R}; J_{\frac{d}{2}}(x) = 0\}, \\ \mathcal{O}(R^d) & \text{as } k \rightarrow 0, \\ \mathcal{O}\left(\frac{1}{k^d(Rk)^{2/3}}\right) & \text{as } k \rightarrow \infty. \end{cases}
 \end{aligned}$$

The two bounds respectively come from the fact that $J_\nu(x) \sim \frac{1}{\Gamma(\nu+1)}(\frac{x}{2})^\nu$ in the neighborhood of zero, and that for all $\nu > 0$ and $x \in \mathbb{R}$, $|J_\nu(x)| \leq c|x|^{-1/3}$ (with $c \approx 0.8$) (Landau, 2000). Thus, for the estimator (38), we let the set of allowed wavenumbers associated to the window $W = B^d(\mathbf{0}, R)$ be

$$\mathbb{A}_R = \left\{ \frac{x}{R} \in \mathbb{R}, \text{ s.t. } J_{d/2}(x) = 0 \right\}. \quad (40)$$

Proposition 2 *Under Assumption A2, for $k \in \mathbb{A}_R$, the estimator \widehat{S}_{BI} is asymptotically unbiased, i.e.,*

$$\sup_{k \in \mathbb{A}_R} \left| \mathbb{E} \left[\widehat{S}_{\text{BI}}(k) \right] - S(k) \right| \xrightarrow{R \rightarrow \infty} 0.$$

Note that we can also define debiased tapered and multitapered versions of Bartlett's estimator, as done in Section 3.1, but the choice of the taper(s) requires more attention, as they must be separable and radial.

3.2.2 Using Ogata's quadrature

Still working under Assumption A2, we can define alternative estimators of the structure factor (11) by first approximating the pair correlation function from a realization of \mathcal{X} , and then approximating the Hankel transform (4).

Estimators of the pair correlation function have been thoroughly investigated; see (Baddeley et al., 2015). In a nutshell, they divide in, on one side, numerical derivatives of estimates of Ripley's K function, and on the other side, direct kernel density estimators based on the collection of pairwise distances in the sample. Both families come with sophisticated edge correction techniques, and, at least for small sample sizes, it seems reasonable to build on this previous work. Henceforth, we assume that an estimator of the pair correlation function is available, and defer the discussion of which estimator to use to Section 5.

It remains to perform a numerical quadrature on a Hankel transform. Ogata (2005) approximates integrals of the form

$$\mathcal{I}_\nu(f) = \int_0^\infty f(x) J_\nu(x) dx$$

as

$$\pi \sum_{j=1}^{\infty} w_{\nu,j} f\left(\frac{\pi}{h} \psi(h\xi_{\nu,j})\right) J_\nu\left(\frac{\pi}{h} \psi(h\xi_{\nu,j})\right) \psi'(h\xi_{\nu,j}), \quad (41)$$

with $w_{\nu,j} = \frac{Y_\nu(\pi\xi_{\nu,j})}{J_{\nu+1}(\pi\xi_{\nu,j})}$ and $\psi(t) = t \times \tanh(\frac{\pi}{2} \sinh(t))$. Y_ν is the Bessel function of the second kind of order ν , h is a positive constant called the *stepsizes*, and $(\xi_{\nu,j})_{j \geq 1}$ are the positive zeros of the Bessel function $J_\nu(\pi x)$ of the first

kind of order ν , arranged in increasing order. In practice, the infinite sum on the right-hand side of (41) can be truncated at a small number of function evaluations since the quadrature nodes approach the zeros of $J_\nu(x)$, that is $\frac{\pi}{h}\psi(h\xi_{\nu,j}) \sim \pi\xi_{\nu,j}$, very fast as $j \rightarrow \infty$.

Ogata's quadrature applies to the Hankel transform (3) of an integrable function f , since

$$\mathcal{H}_\nu(f)(k) = \mathcal{I}_\nu \left(x \mapsto \frac{x}{k^2} f(x/k) \right). \quad (42)$$

In particular, it applies to the computation of structure factors since, by (11) and (4),

$$\begin{aligned} S(k) &= 1 + \rho \mathcal{F}_s(g-1)(k) \\ &= 1 + \rho \frac{(2\pi)^{d/2}}{k^{d/2-1}} \mathcal{I}_{d/2-1} \left(x \mapsto \frac{x^{d/2}}{k^{d/2+1}} g(x/k) - 1 \right). \end{aligned}$$

We thus define the Hankel-Ogata estimator of the structure factor as

$$\widehat{S}_{\text{HO}}(k) = 1 + \rho \frac{(2\pi)^{d/2} \pi}{k^\nu} \sum_{j=1}^N w_{\nu,j} \tilde{h}_k \left(\frac{\pi}{h} \psi(h\xi_{\nu,j}) \right) J_\nu \left(\frac{\pi}{h} \psi(h\xi_{\nu,j}) \right) \psi'(h\xi_{\nu,j}), \quad (43)$$

with $\nu = d/2 - 1$, $N \in \mathbb{N}$, $\tilde{h}_k(x) = \frac{x^{d/2}}{k^{d/2+1}}(\hat{g}(x/k) - 1)$, and \hat{g} an estimator of the pair correlation function. Finally, note that Ogata's quadrature is also implemented in the Python package [hankel](#) of [Murray and Poulin \(2019\)](#).

Relation between k_{\min} and r_{\max}

There exists a hidden inverse proportionality relation in Equation (43), between the minimal wavenumber k_{\min} for which we can hope the estimator to be accurate and the maximal radius r_{\max} at which the pair correlation function has been estimated. Truncating the infinite sum after N terms in Equation (41) has been informally justified by

$$\psi(h\xi_{d/2-1,N}) \approx h\xi_{\frac{d}{2}-1,N} \quad (44)$$

The maximum radius r_{\max} at which \hat{g} is available should in turn satisfy

$$r_{\max} = \max_j \left\{ \frac{\pi}{hk} \psi(h\xi_{\frac{d}{2}-1,j}); k \in \mathbb{R}^* \right\} \quad (45)$$

Together, (44) and (45) entail that

$$k_{\min} \approx \frac{\pi\xi_{d/2-1,N}}{r_{\max}}. \quad (46)$$

Thus k_{\min} is not only proportional to $1/r_{\max}$ but also to the largest considered zero of the Bessel function $J_{d/2-1}(x)$.

3.2.3 Using the quadrature of Baddour and Chouinard

Instead of using the quadrature of [Ogata \(2005\)](#), one can estimate Hankel transforms more directly, similarly to how the discrete Fourier transform is used to approximate Fourier transforms. Intuitively, assuming that either f or its Hankel transform $\mathcal{H}_\nu(f)$ (3) has bounded support allows rewriting it as a Fourier-Bessel series, with coefficients involving evaluations of either $\mathcal{H}_\nu(f)$ or f , respectively. Truncating the resulting Fourier-Bessel series yields approximate direct and inverse Hankel transforms. This discrete Hankel transform (DHT) was derived by [Baddour and Chouinard \(2015\)](#), and originally implemented in [Matlab](#). Moreover, [Guizar-Sicairo and Gutiérrez-Vega \(2004\)](#) developed a [Python](#) package, [pyhank](#), based on the same idea.

In detail, let $N > 0$ and $f : \mathbb{R}^+ \rightarrow \mathbb{R}$ be a continuous function, [Baddour and Chouinard \(2015\)](#) approximate

$$\mathcal{H}_\nu(f)(k_m) \approx \frac{r_{\max}^2}{\eta_{\nu,N}} \sum_{j=1}^{N-1} \frac{2J_\nu\left(\frac{\eta_{\nu,m}\eta_{\nu,j}}{\eta_{\nu,N}}\right) f(r_j)}{\eta_{\nu,N} J_{\nu+1}^2(\eta_{\nu,j})}, \quad (47)$$

where $\eta_{\nu,m} = \pi\xi_{\nu,m}$ is the m^{th} positive zero of the Bessel function $J_\nu(x)$ of the first kind, $1 \leq j, m \leq N-1$ and

$$r_j = \frac{\eta_{\nu,j}}{\eta_{\nu,N}} r_{\max}, \quad k_m = \frac{\eta_{\nu,m}}{\eta_{\nu,N}} k_{\max}, \quad k_{\max} = \frac{\eta_{\nu,N}}{r_{\max}}, \quad \text{with } r_{\max} > 0. \quad (48)$$

The user thus needs to specify both N and r_{\max} . Intuitively, the choice of r_{\max} is governed by how far on the positive axis one has been able to evaluate f . Once r_{\max} is fixed, N decides how large k_{\max} is, that is, how high in frequency one wishes to estimate the Hankel transform.

To conclude, given an estimator \hat{g} of the pair correlation function, we define yet another estimator of the structure factor, called the Hankel-Baddour-Chouinard estimator,

$$\hat{S}_{\text{HBC}}(k_m) = 1 + \rho(2\pi)^{\frac{d}{2}} \frac{r_{\max}^2}{\eta_{\nu,N}} \sum_{j=1}^{N-1} \frac{2J_\nu\left(\frac{\eta_{\nu,m}\eta_{\nu,j}}{\eta_{\nu,N}}\right)}{\eta_{\nu,N} J_{d/2}^2(\eta_{\nu,j})} \tilde{h}(r_j) k_m^\nu, \quad (49)$$

where $\nu = d/2 - 1$, $\tilde{h}(x) = x^\nu(\hat{g}(x) - 1)$, and the set of wavenumbers $\{k_m\}_m$ is fixed by (48). Finally, we can deduce from (48) that the minimal wavenumber of \hat{S}_{HBC} (49) is $k_1 = k_1^{d/2-1} = \frac{\eta_{d/2-1,1}}{r_{\max}}$. Comparing k_1 with the minimal wavenumber k_{\min} (46) of \hat{S}_{HO} (43), for the same number of points N and the same r_{\max} , we observe that $k_1 < k_{\min}$, as k_1 is proportional to the first zero of the Bessel function $J_{d/2-1}(x)$ while k_{\min} is proportional to the N^{th} zero of $J_{d/2-1}(x)$. For the study of hyperuniformity, this suggests an advantage to using \hat{S}_{HBC} .

4 Statistical hyperuniformity test

In Section 3, we have surveyed estimators \widehat{S} of the structure factor S of a stationary point process \mathcal{X} . In the best case, we had an asymptotically unbiased estimator of S . Furthermore, hyperuniformity diagnostics like the effective hyperuniformity surveyed in Section 2.5 require subjective algorithmic choices and do not come with a statistical guarantee.

In this section, we use the debiasing device of Rhee and Glynn (2015) to turn realizations of any of the positive asymptotically unbiased estimators of Section 3, on windows of increasing size, into an unbiased estimator of a truncated equivalent to $S(\mathbf{0})$. We then propose the first asymptotically valid test of hyperuniformity. We group our assumptions and notation for this section in Assumption A3.

Assumption A3 \mathcal{X} is a stationary point process of \mathbb{R}^d with intensity $\rho > 0$. Its pair correlation function g exists, and $\mathbf{r} \mapsto g(\mathbf{r}) - 1$ is integrable on \mathbb{R}^d .

4.1 The coupled sum estimator

Consider a stationary point process \mathcal{X} of \mathbb{R}^d , of which we observe the intersection of a single realization with multiple increasing windows. Formally, we consider an increasing sequence of sets $(\mathcal{X} \cap W_m)_{m \geq 1}$, with $W_s \subset W_r$ for all $0 < s < r$, and $W_\infty = \mathbb{R}^d$. For simplicity, we assume that the windows are centered and either rectangular as in Assumption A1, or ball-shaped as in Assumption A2 if \mathcal{X} is isotropic.

We consider any of the positive, asymptotically unbiased estimators \widehat{S}_m of S listed in Section 3, applied to $\mathcal{X} \cap W_m$. All such estimators are asymptotically unbiased on a set of values \mathbb{B}_m , possibly in the sense of Proposition 1, and there exists $\mathbf{k}_m^{\min} \in \mathbb{B}_m$ with $\mathbf{k}_m^{\min} \rightarrow \mathbf{0}$. The reader can keep in mind the scattering intensity of Section 3.1.1, with, say, the minimum restricted allowed value $\mathbf{k}_m^{\min} = (2\pi/L_{m_1}, \dots, 2\pi/L_{m_d}) \in \mathbb{Z}^d$, but the proofs hold more generally.

We define the sequence of random variables

$$Y_m = 1 \wedge \widehat{S}_m(\mathbf{k}_m^{\min}), \quad m \geq 1, \tag{50}$$

We cap the estimators at 1 arbitrarily to make them uniformly bounded. The idea is to use the sequence (Y_m) to test whether $S(\mathbf{0}) = 0$.

Following (Rhee and Glynn, 2015, Section 2), we first define a new sequence

$$Z_m = \sum_{j=1}^{m \wedge M} \frac{Y_j - Y_{j-1}}{\mathbb{P}(M \geq j)}, \quad m \geq 1, \tag{51}$$

where M is an \mathbb{N} -valued random variable such that $\mathbb{P}(M \geq j) > 0$ for all j , and $Y_0 = 0$ by convention. Rhee and Glynn (2015) observed that

$$\mathbb{E}[Z_m] = \mathbb{E}[Y_m] \quad \text{and} \quad Z_m \xrightarrow[m \rightarrow \infty]{\text{a.s.}} Z,$$

where Z is the *coupled sum estimator*

$$Z = \sum_{j=1}^M \frac{Y_j - Y_{j-1}}{\mathbb{P}(M \geq j)}. \quad (52)$$

Under some conditions, Rhee and Glynn (2015) proved that if $Y_m \rightarrow Y$ in L^2 , then $Z \in L^2$ is an unbiased estimator of $\mathbb{E}[Y]$ with a square root convergence rate. For our choice of $(Y_m)_m$, the assumptions of (Rhee and Glynn, 2015, Theorem 1), especially the L^2 convergence of Y_m , may not hold for non-hyperuniform point processes. We thus use weaker assumptions that are still enough to build a hyperuniformity test.

Proposition 3 *Under Assumption A3, with Z defined in (52), assume that $M \in L^p$ for some $p \geq 1$. Then $Z \in L^p$ and $Z_m \rightarrow Z$ in L^p . Moreover,*

1. *If \mathcal{X} is hyperuniform, then $\mathbb{E}[Z] = 0$.*
2. *If \mathcal{X} is not hyperuniform and*

$$\sup_m \mathbb{E}[\widehat{S}_m^2(\mathbf{k}_m^{\min})] < \infty, \quad (53)$$

then $\mathbb{E}[Z] \neq 0$.

The proof is deferred to Appendix A. Assumption (53) bears on the estimator that we use for the structure factor and the point process. We believe it not to be too strong and we prove it in Appendix B for the scattering intensity for a Poisson point process. Proposition 3 naturally leads to a test of hyperuniformity.

4.2 Hyperuniformity multiscale test

We apply Proposition 3 with $p = 2$, say M is a Poisson random variable with mean $\lambda > 0$. Then $\text{Var}[Z] < \infty$, and we can apply the central limit theorem to build a standard test comparing $\mathbb{E}[Z]$ to zero.

Consider A i.i.d. pairs $(\mathcal{X}_a, M_a)_{a=1}^A$ of realizations of (\mathcal{X}, M) , and let Z_1, \dots, Z_A be the A corresponding i.i.d. copies of Z . Now, denote the sample mean and sample standard deviation of Z by \bar{Z}_A and $\bar{\sigma}_A$. Since the variance of Z is finite, Slutsky's lemma yields the usual asymptotic confidence interval $CI[\mathbb{E}[Z]]$ of level ζ for $\mathbb{E}[Z]$,

$$\left[\bar{Z}_A - z \bar{\sigma}_A A^{-1/2}, \bar{Z}_A + z \bar{\sigma}_A A^{-1/2} \right], \quad (54)$$

where z is chosen such that $\mathbb{P}(-z < \mathcal{N}(0, 1) < z) = \zeta$, and $\mathcal{N}(0, 1)$ denotes the standard normal distribution. By Proposition 3, for an estimator of the structure factor satisfying (53), a test of hyperuniformity of asymptotic level ζ consists in assessing whether 0 lies in the interval (54). Since the estimators Z correspond to windows of different sizes, we call the test *multiscale*.

5 Demonstrating all estimators using our toolbox

We have implemented all estimators of Section 3, as well as the regression diagnostics of Section 2.5, in an open-source Python toolbox called [structure_factor](#)⁴.

In this section, we quickly demonstrate the toolbox on the four point processes described in Section 2.6, that is, the KLY process of intensity $\rho_{\text{KLY}} = 1$, the Ginibre ensemble of intensity $\rho_{\text{Ginibre}} = 1/\pi$, the Poisson process of intensity $\rho_{\text{Poisson}} = 1/\pi$, and the Thomas process with intensity $\rho_{\text{Thomas}} = 1/\pi$, $\rho_{\text{parent}} = 1/(20\pi)$ and $\sigma = 2$. Our choice of observation window depends on the intensity and makes sure that we get samples of around 5800 points. The dimension is always $d = 2$. All figures in this section can be reproduced by following our demonstration [notebook](#) ⁵.

5.1 Basic software objects

While we refer to our online [documentation](#)⁶ for details, we believe that a quick overview of the main objects of our package is useful. All estimators from Section 3 are methods of the class `StructureFactor`. The class constructor takes as input an object of type `PointPattern`. In a nutshell, for a stationary point process \mathcal{X} of intensity ρ , a `PointPattern` encapsulates a sample of $\mathcal{X} \cap W = \{x_1, \dots, x_N\}$, the observation window W , and the intensity ρ (optional). If the intensity of \mathcal{X} is not provided by the user, it is automatically approximated by the asymptotically unbiased estimator $\hat{\rho} = \frac{N}{|W|}$. Finally, to comply with the requirements of estimators on specific windows, we provide a `restrict_to_window()` method for the class `PointPattern`.

5.2 Demonstrating estimators that only assume stationarity

The scattering intensity

Figure 3 illustrates the scattering intensity estimator of Section 3.1. Columns respectively correspond to the KLY, Ginibre, Poisson, and Thomas point processes. The first row contains a sample of each point process, observed in square windows. The second row shows the scattering intensity \hat{S}_{SI} in (23) on arbitrary wavevectors \mathbf{k} , while in the third row, the estimators are only evaluated on a subset of the allowed wavevectors (22). The fourth and fifth rows

⁴<https://github.com/For-a-few-DPPs-more/structure-factor>

⁵<https://github.com/For-a-few-DPPs-more/structure-factor/tree/main/notebooks>

⁶<https://for-a-few-dpps-more.github.io/structure-factor/>

Point process

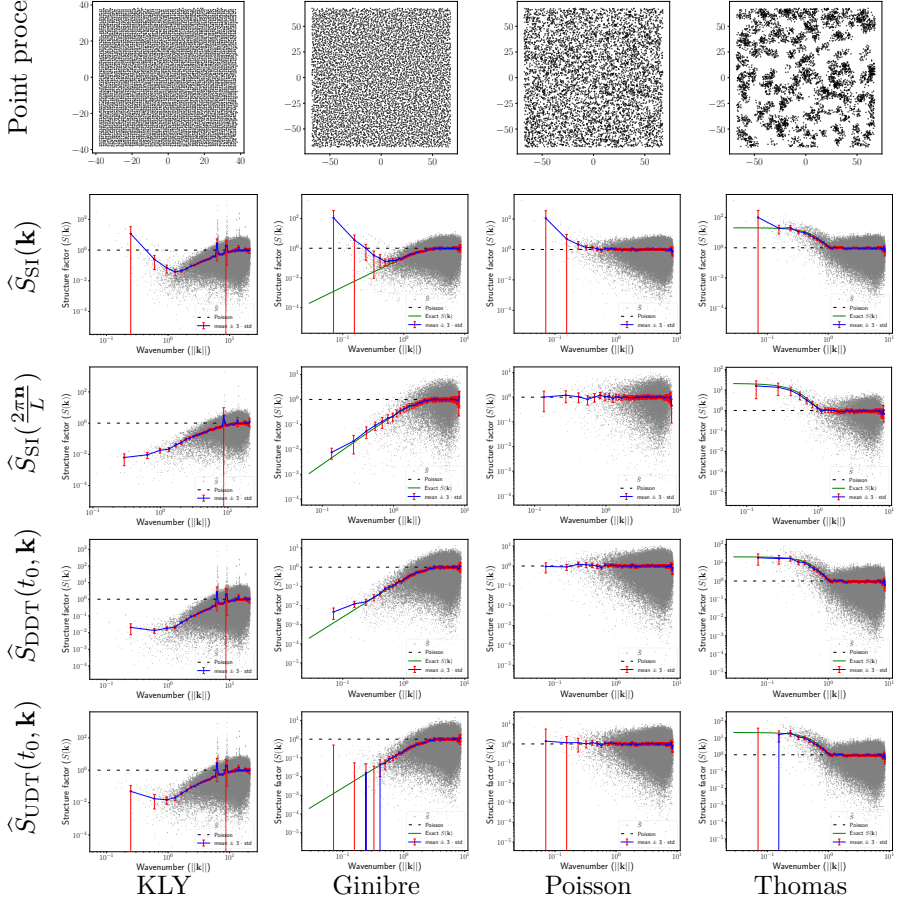


Fig. 3: Variants of the scattering intensity estimator applied to four point processes. The computation and visualization are done using `structure_factor` (see Section 5.2 for details)

illustrate the debiasing techniques, respectively the directly debiased scattering intensity $\widehat{S}_{DDT}(t_0, \mathbf{k})$ from (32), and the undirectly debiased scattering intensity $\widehat{S}_{UDT}(t_0, \mathbf{k})$ from (31).

The clouds of grey points are the approximated structure factors. Note that since all benchmark point processes are (at least approximately) isotropic, the structure factor S is a radial function, so we plot $k \mapsto \widehat{S}(k)$, $k \in \mathbb{R}$, and not $\mathbf{k} \mapsto \widehat{S}(\mathbf{k})$, $\mathbf{k} \in \mathbb{R}^2$. To regularize the obtained estimator, we bin the norm of the wavevectors regularly and provide the empirical mean (in blue) and the empirical standard deviation of the mean (red bars indicate ± 3 such standard deviations). Note that the binning can be specified by the user in our library. On each plot, the exact structure factor is represented by a green line when

it is known. Finally, the dashed black lines are the structure factor of the homogeneous Poisson process, for reference.

While we refer to Section 6 for a more detailed comparison, one can already observe from Figure 3 that the most accurate estimators are the scattering intensity \widehat{S}_{SI} (23) evaluated on the set of allowed wavevectors (22) and the debiased scattering intensity $\widehat{S}_{\text{DDT}}(t_0, \mathbf{k})$ (32). The bias at small, non-allowed wavenumbers of the scattering intensity is visible in the second row. As for the undirectly debiased variant, it produces a few negative values, visible as large error bars on our log-log plot.

Using an alternate taper

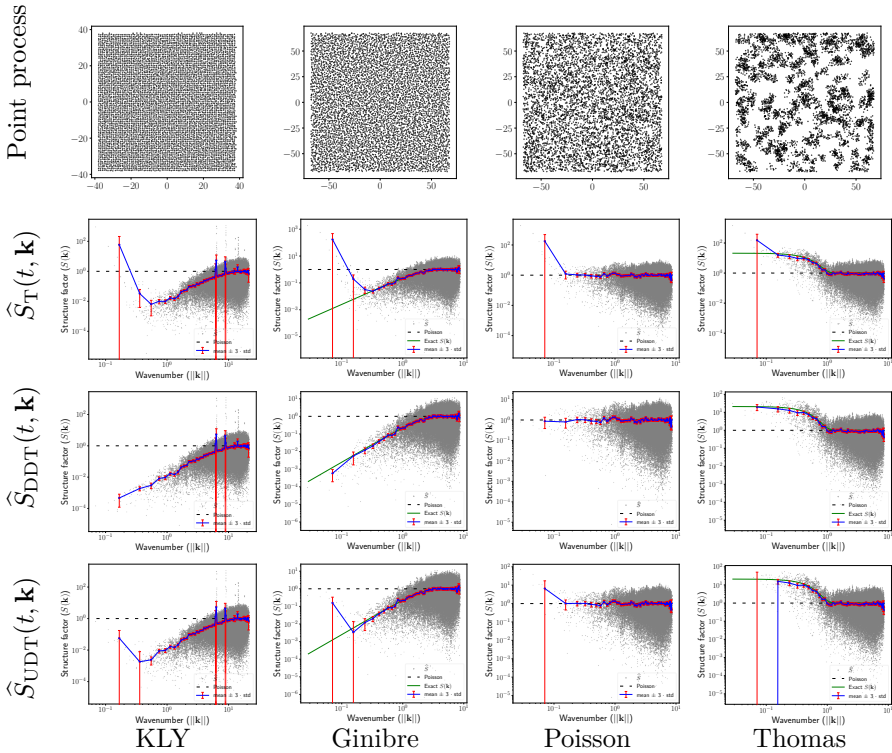


Fig. 4: Tapered estimator and the corresponding debiased versions: KLY process (first column), Ginibre ensemble (second column), Poisson process (third column), and Thomas process (last column). The computation and visualization are done using `structure_factor`

Now, as mentioned in Section 3, the scattering intensity \widehat{S}_{SI} is a particular case of the tapered estimator \widehat{S}_{T} , with the specific taper t_0 . We are free to use other tapers verifying (29).

Figure 4 shows the estimated structure factors of the same four benchmark point processes (first row), using \widehat{S}_T (second row), the corresponding directly debiased version \widehat{S}_{DDT} (third row), and the undirectly debiased version \widehat{S}_{UDT} (last row). The taper used is the first sinusoidal taper $t_1(\mathbf{x}, W) = t(\mathbf{x}, \mathbf{p}^1, W)$ with $\mathbf{p}^1 = (1, 1)$ in (34). The same legend applies as for Figure 3.

First, the asymptotic bias of \widehat{S}_T at small wavenumber k is visible in the second row. Second, for the KLY process (first column), the Ginibre ensemble (second column), and the Poisson process (third column) the estimator \widehat{S}_{UDT} (last row) returned a few negative values again, resulting in large inaccuracies in our log-log scale. The directly debiased estimator \widehat{S}_{DDT} yields the most accurate approximation of known structure factors, consistently across point processes.

Averaging over multiple tapers

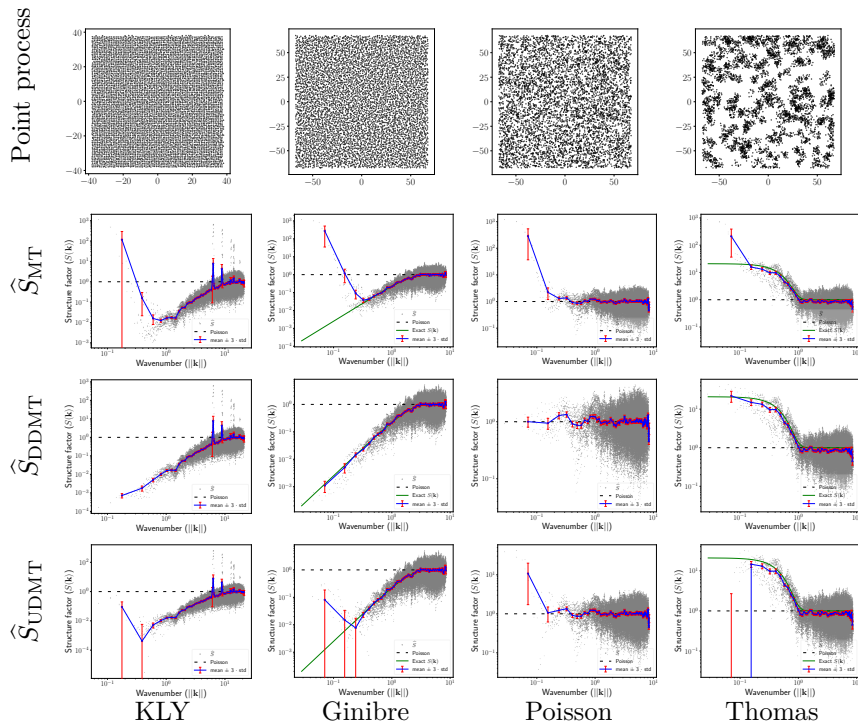


Fig. 5: Multitapered estimator and the debiased versions: KLY process (first column), Ginibre ensemble (second column), Poisson process (third column), and Thomas process (last column). The computation and visualization are done using `structure_factor`

The multitapered estimator \widehat{S}_{MT} of (33) is now investigated in Figure 5, using the first four sinusoidal tapers, i.e., $(t_q)_{q=1}^4$ with $t_q(\mathbf{x}, W) = t(\mathbf{x}, \mathbf{p}^q, W)$ and $\mathbf{p}^q \in \{1, 2\}^2$ in (34). We also show the results of the corresponding directly and undirectly debiased versions, $\widehat{S}_{\text{DDMT}}$ and $\widehat{S}_{\text{UDMT}}$. We again observe the bias of \widehat{S}_{MT} at small wavenumbers (second row), and that the negative values output by $\widehat{S}_{\text{UDMT}}$ at small wavenumbers (last row) make visual assessments of hyperuniformity less straightforward. Like with single tapers, the directly debiased estimator $\widehat{S}_{\text{DDMT}}$ gives a consistently accurate approximation. Compared to Figure 4, however, it is not obvious whether multitapering yields a smaller mean square error than single tapers, and a more quantitative study will investigate this in Section 6.

5.3 Demonstrating estimators that assume isotropy

Bartlett's isotropic estimator

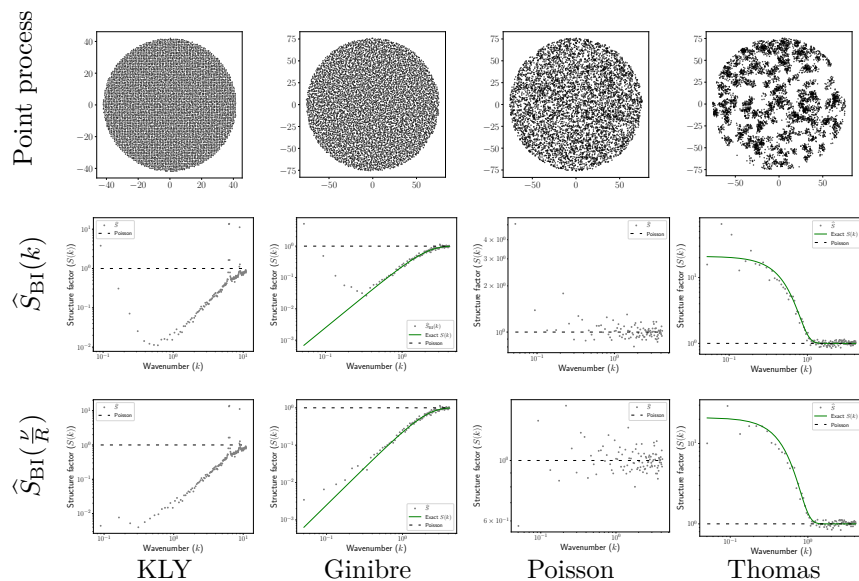


Fig. 6: Bartlett's isotropic estimator: KLY process (first column), Ginibre ensemble (second column), Poisson process (third column), and Thomas process (last column). The computation and visualization are done using `structure_factor`

Figure 6 illustrates Bartlett's isotropic estimator of Section 3.2. Columns respectively correspond to the KLY, Ginibre, Poisson, and Thomas point processes. The first row contains a sample of each point process, observed in ball windows. The second row shows \widehat{S}_{BI} on arbitrary wavenumbers k , while in

the last row, the estimator is only evaluated on a subset of the Bessel-specific allowed wavenumbers (40).

First, we note that, unlike scattering intensity variants, plotting Bartlett’s isotropic estimator $k \mapsto \widehat{S}_{\text{BI}}(k)$ in (38) does not require binning. On the other hand, Bartlett’s estimator is significantly costlier than its scattering intensity counterpart; See Section 6.1. Now, we comment on the accuracy of the estimator in Figure 6. Here again, small, non-allowed wavenumbers give rise to large biases for $\widehat{S}_{\text{BI}}(k)$, especially for the two hyperuniform point processes (KLY and Ginibre). When applied to allowed wavenumbers, the estimator shows accuracy across all point processes, similarly to the directly debiased tapered estimators.

Estimating the pair correlation function

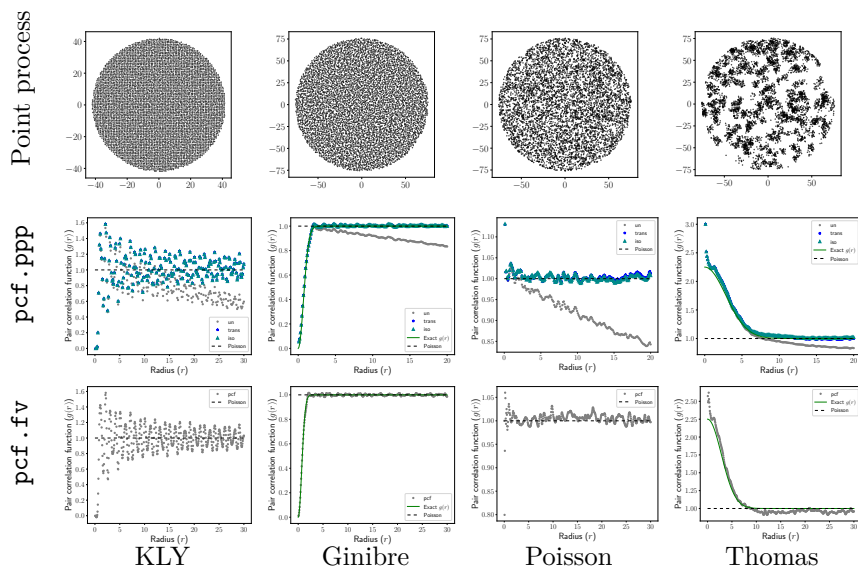


Fig. 7: Approximated pair correlation function: KLY process (first column), Ginibre ensemble (second column), Poisson process (third column), and Thomas process (last column). The computation and visualization are done using `structure.factor`

The last two estimators of the structure factor are \widehat{S}_{HO} in (43) and \widehat{S}_{HBC} in (49). These estimators require an approximation of the pair correlation function (pcf) of the point process. We thus quickly investigate standard estimators of the pcf on our benchmark point processes.

There are two types of estimators of the pcf for stationary isotropic point processes (Baddeley et al., 2015): kernel density estimators applied to pairwise distances and numerical derivatives of Ripley’s K function. The R library

`spatstat` implements both, respectively as `pcf.ppp`, which uses an Epanechnikov kernel and Stoyan’s rule of thumb for bandwidth selection (Baddeley et al., 2015, Section 7.6.2), and `pcf.fv`, which computes the derivative of a polynomial estimator of Ripley’s K function. The kernel density estimator behaves badly for small values of r : for many point processes, its variance becomes infinite when r goes to 0. The derivative estimator is recommended for large datasets, where direct estimation of the pcf can be time-consuming (Baddeley et al., 2015, Section 7.6.2). Figure 7 shows the two estimators of the pair correlation function of the benchmark point processes. Note that we provide an independent, open-source Python interface⁷ to the R library `spatstat`. The second row shows the estimation of the pair correlation function using `pcf.ppp`. This method provides a choice of boundary corrections, like `"trans"`, `"iso"`, or none (`"un"`). For more details see Baddeley et al. (2015, Sections 7.4.4 and 7.4.5). The last row of Figure 7 shows the estimation of the pair correlation function using `pcf.fv`.

We observe that, for the cardinalities considered here, the choice of edge correction method is irrelevant, as long as there is one. We also observe that the two methods for estimating the pcf perform similarly, and we pick `pcf.fv` for the rest of this section. We manually remove undefined values (`NaN`, `-Inf`, or `Inf`), and we interpolate the obtained discrete approximation of g , in order to evaluate it at any point required by the quadratures of Section 3.2.2, and 3.2.3. Finally, note that the maximum radius r_{\max} at which `spatstat` provides an approximation of g is limited by the size of the observation window. Typically, it should be less than half the window diameter for a ball window, and less than 1/4 of the smaller side length of the window for a rectangular window; see the [documentation](#) of `spatstat`. For larger values than the r_{\max} provided by `spatstat`, we manually set g to be identically 1, which has the effect of automatically truncating quadratures that evaluate $g-1$, like Ogata’s quadrature (43).

Hankel transform quadratures

Figure 8 shows the results of Ogata’s \widehat{S}_{HO} (second row) and Baddour-Chouinard’s \widehat{S}_{HBC} (last row) on our four benchmark point processes from Section 2.1. The legend is the same as for Figure 3; see Section 5.2. For the accuracy of the estimators, we can see that \widehat{S}_{HO} failed to approximate the structure factor of the KLY process. Even the results of \widehat{S}_{HBC} seem to be unreliable. The non-isotropy of the KLY process may be the reason for the fluctuations of its approximated pair correlation function in Figure 7, leading to the inaccuracies of the quadratures. For the remaining point processes, \widehat{S}_{HBC} seems to give more accurate results than \widehat{S}_{HO} .

⁷At <https://github.com/For-a-few-DPPs-more/spatstat-interface> and on PyPI.

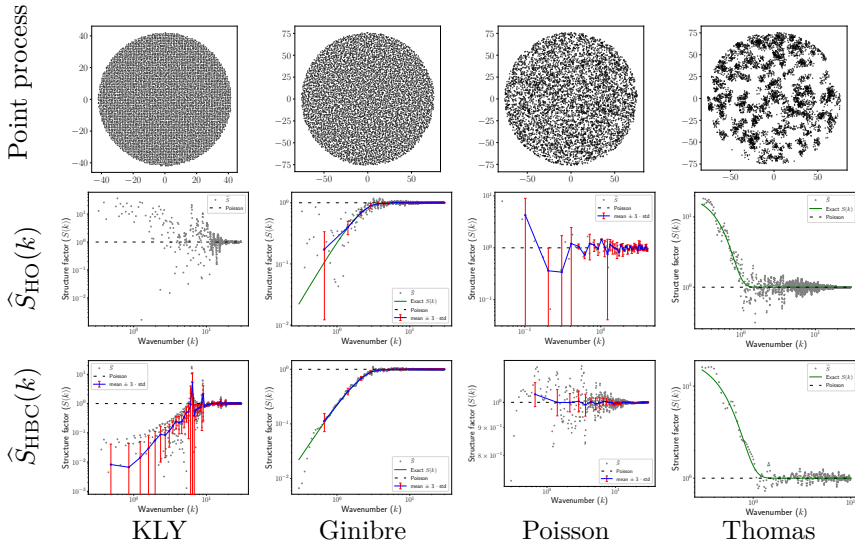


Fig. 8: Estimation using Hankel transform quadratures: KLY process (first column), Ginibre ensemble (second column), Poisson process (third column), and Thomas process (last column). The computation and visualization are done using `structure_factor`

5.4 Hyperuniformity diagnostics

We now demonstrate the estimation of the hyperuniformity index H from Section 2.5, the multiscale hyperuniformity test from Section 4, and the estimation of the decay rate α from Section 2.4.

Effective hyperuniformity

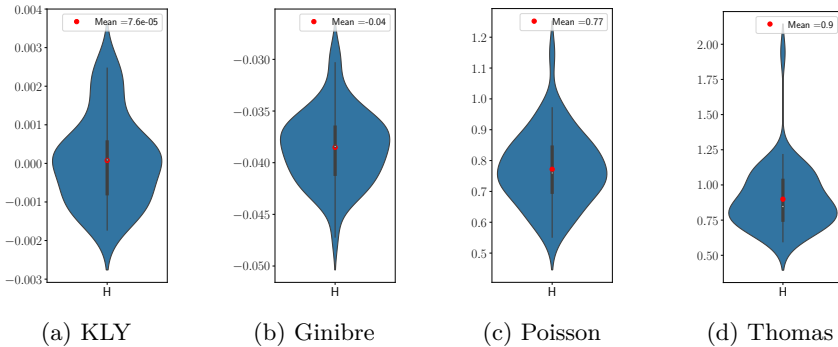


Fig. 9: Violin plots of H across 50 samples from the KLY, Ginibre, Poisson, and Thomas point process. The computation is done using `structure_factor`

Figure 9 illustrates the violin plots of H across 50 samples from the benchmark point processes. We used the results of \widehat{S}_{BI} , across 50 samples of roughly 10^4 points each (see Section 5.3). To fit the line required to compute H , we considered the wavenumbers up to 0.6 for the Thomas process and 1 for the remaining point processes. These values were chosen manually: the trade-off is to remain close to zero while including enough data points to fit a line. The violin plots of Figure 9 indicate that, consistently across realizations of the Poisson and Thomas point processes, H is larger than, say, 0.5. This is a strong hint that these point processes are not hyperuniform. On the contrary, for Ginibre, H is even slightly negative, hinting at hyperuniformity. For the KLY process, although H is close to zero, we note that a threshold of 10^{-3} would not lead to the same answer across all 50 realizations.

Multiscale hyperuniformity test

Table 2: Multiscale hyperuniformity test

| | \bar{Z}_{50} | $CI[\mathbb{E}[Z]]$ | \bar{Z}_{50} | $CI[\mathbb{E}[Z]]$ |
|---------------|---------------------------|---------------------|---------------------------|---------------------|
| KLY | 0.003 | [-0.003, 0.009] | 0.003 | [-0.0003, 0.007] |
| Ginibre | 0.015 | [-0.021, 0.051] | 0.007 | [-0.003, 0.011] |
| Poisson | 0.832 | [0.444, 1.220] | 0.781 | [0.560, 1.001] |
| Thomas | 0.928 | [0.788, 1.068] | 1 | [0.999, 1] |
| \widehat{S} | \widehat{S}_{SI} | | \widehat{S}_{BI} | |

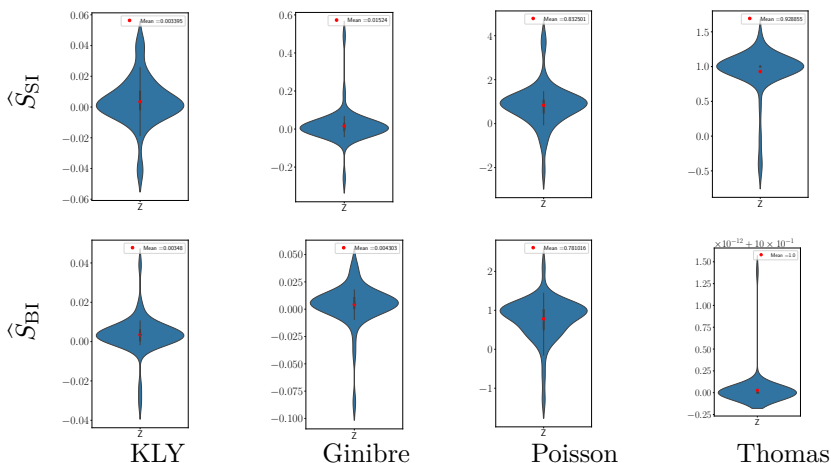


Fig. 10: Violin plots of Z across 50 samples from the KLY, Ginibre, Poisson, and Thomas point process using \widehat{S}_{SI} (first line) and \widehat{S}_{BI} (last line). The computation is done using `structure_factor`

Table 2 summarizes the results of the multiscale hyperuniformity test of Section 4.2, for the scattering intensity and Bartlett’s isotropic estimators, on rectangular windows for the former and ball windows for the latter. To compute \bar{Z}_A , we used $A = 50$ draws of (\mathcal{X}_a, M_a) . In practice, the Ginibre ensemble cannot be sampled on arbitrarily large windows on a personal computer. We thus proceed as follows. Let L_{\max} , respectively R_{\max} , be the maximum sidelength of the box- (respectively ball-) shaped window on which the point process can be sampled in practice. Since M_a is Poisson with parameter λ , we choose λ such that the probability that W_{M_a} is larger than $W_{L_{\max}}$ (respectively $W_{R_{\max}}$) is smaller than 10^{-4} . Precisely, for the scattering intensity, $\lambda = 85$, and the sidelength of the box window ranges from $L_{\min} = 20$ to $L_{\max} = 140$, with a unit stepsize for the Ginibre, the Poisson and the Thomas process. The wavevectors used $\{\mathbf{k}_m^{\min}\}_{m \geq 1}$ are the minimum wavevectors of (24) corresponding to $\{W_m\}_{m \geq 1}$. Finally, the asymptotic confidence interval (54), denoted by $CI[\mathbb{E}[Z]]$ in Table 2, has a 99.7% asymptotic level since we use three standard deviations. For Bartlett’s estimator, we use ball windows with a minimum radius $R_{\min} = 30$, a maximum radius $R_{\max} = 100$, a unit step size, $\lambda = 50$, and the minimum wavenumbers of (40) corresponding to the subwindows for the Ginibre, the Poisson and the Thomas process. For the KLY process having bigger intensity than the other benchmarks point processes, we use smaller parameters $L_{\max} = 80$, $R_{\max} = 56$ and $L_0 = R_0 = 20$.

We can see from Table 2 that the test successfully rejects hyperuniformity for the Poisson and Thomas point processes, and does not reject for the Ginibre and the KLY process, as expected. Moreover, we note that \hat{S}_{BI} provides tighter confidence intervals.

Note that the coverage of the confidence interval on which our test is based is only controlled when A goes to infinity. For a fixed λ , we thus recommend choosing A as large as possible. In particular, the overly wide confidence interval for the Poisson process in Table 2 calls for increasing A . Indeed, the violin plot of the 50 realizations of Z (Figure 10) has large support. Increasing A naturally reduces the size of that support; see Figure 11. Note in passing how \bar{Z}_A does not converge to $S(\mathbf{0}) = 1$, which is an effect of our capping the estimated structure factor in (50). Overall, there is no free lunch: our test might

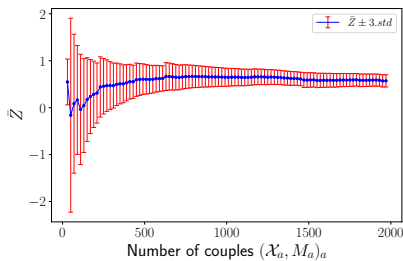


Fig. 11: $CI[\mathbb{E}[\bar{Z}]]$ for a Poisson point process with the scattering intensity, as a function of the number of realizations of Z .

fail in diagnosing hyperuniformity if A or λ is too small.

Hyperuniformity class

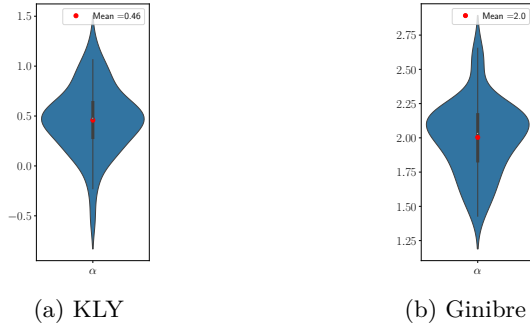


Fig. 12: Violin plots of α across 50 samples of the KLY and the Ginibre point process. The computation is done using `structure_factor`

Figure 12 shows the violin plots of the estimated power decay α across 50 samples, of roughly 10^4 points each, of the KLY and the Ginibre point processes. We used the results of \widehat{S}_{BI} . To approximate the decay rate α of the structure factor, the maximum wavenumber used to fit the polynomial is equal to 0.45 for the Ginibre ensemble, and to 0.6 for the KLY process. Again, these thresholds are fit manually and represent a trade-off between having enough points to fit our monomial and being close to zero. Results are shown in Figure 12. There is limited evidence that the KLY process is indeed hyperuniform: while the support of the distribution is large and includes 0, most estimated values of α are positive, and concentrate around 0.5. This is a hint that KLY might belong to Class III in Table 1. For the Ginibre ensemble, the concentration of values of α around 2 successfully reflects the known power decay (Section 2.1).

6 A quantitative comparison of the estimators

We now compare the cost and accuracy of all estimators more quantitatively.

6.1 A note on computational costs

For a given wavevector, evaluating any single-tapered estimator requires a sum of N terms. Multitapering naturally multiplies the cost by the number of tapers, but it can be trivially parallelized, especially since the number of tapers remains low in practice (Rajala et al., 2020).

On the other hand, for a sample of N points, Bartlett's estimator \widehat{S}_{BI} is a sum of $\mathcal{O}((N^2 - N)/2)$ evaluations of a Bessel function. This makes Bartlett's

estimator significantly costlier than its scattering intensity counterpart. As an example, for a realization of $N = 10^4$ points from a point process in \mathbb{R}^2 , using a modern laptop, the evaluation of \widehat{S}_{SI} at a single wavevector took about one millisecond, compared to 2 seconds for \widehat{S}_{BI} . Note however that for a similar accuracy on an isotropic point process, \widehat{S}_{BI} needs to be evaluated at fewer wavevectors than, say, the scattering intensity. Indeed, a single value of the former should be compared to a binwise average of the latter.

Now, for Hankel quadrature estimators, the main bottleneck is the approximation of the pcf. A kernel density estimator based on N points is again a quadratic computation. In our experience, combining the estimator `pcf.fv`, based on numerically differentiating an estimated Ripley's K function, and a Hankel quadrature to build \widehat{S}_{HO} and \widehat{S}_{HBC} is the least expensive pipeline.

6.2 Measuring the accuracy of the estimators near zero

To confirm the intuitions gained from Section 5, in particular that the multitapered variant of the scattering intensity and Bartlett's estimator dominate the others when it comes to visual diagnostics of hyperuniformity, we now compare the mean square error of the different estimators of the structure factor, integrated near 0.

For a subdivision $[k_1, k_2) \cup \dots \cup [k_{J-1}, k_J)$ of some interval $[k_1, k_J)$, the integrated MSE reads

$$\begin{aligned} \text{iMSE}(\widehat{S}) &= \int_{k_1}^{k_J} \text{MSE}(\widehat{S})(k) dk \\ &= \int_{k_1}^{k_J} \mathbb{E}[\widehat{S}(k) - S(k)]^2 dk \\ &= \mathbb{E} \left[\int_{k_1}^{k_J} [\widehat{S}(k) - S(k)]^2 dk \right]. \end{aligned}$$

A crude numerical integration using the trapezoidal rule gives,

$$\text{iMSE}(\widehat{S}) \approx \mathbb{E} \left[\sum_{j=1}^{J-1} \frac{1}{2} (k_{j+1} - k_j) \left\{ [\widehat{S}(k_{j+1}) - S(k_{j+1})]^2 + [\widehat{S}(k_j) - S(k_j)]^2 \right\} \right], \quad (55)$$

The expectation in (55) is under the investigated point process. Assuming it is easy to sample from the point process, we can estimate the iMSE in (55) by an empirical average $\widehat{\text{iMSE}}$ over point process samples. Similarly, the difference of the iMSEs of two different estimators of S can be approximated by an empirical average of differences of $\widehat{\text{iMSE}}$ s. This yields a natural (paired) Student test to assess whether the difference of the iMSEs of two different estimators of S is 0.

6.3 Comparing variants of the scattering intensity

In Section 5, we derived the intuition that \widehat{S}_{SI} on its allowed values, $\widehat{S}_{\text{DDT}}(t_0, \mathbf{k})$, $\widehat{S}_{\text{DDT}}(t_1, \mathbf{k})$, and $\widehat{S}_{\text{DDMT}}((t_q)_{q=1}^4, \mathbf{k})$ gave the most accurate approximations among the estimators of Section 3. We further expect $\widehat{S}_{\text{DDMT}}((t_q)_{q=1}^4, \mathbf{k})$ to have the smallest integrated MSE among them. To test this, we run three paired, one-sided Student tests, comparing $\widehat{S}_{\text{DDMT}}((t_q)_{q=1}^4, \mathbf{k})$ to each of the three former estimators.

Specifically, we use 50 independent realizations of approximately 5800 points each, from the Ginibre, Poisson, and Thomas point processes, for which we know the exact structure factor. The intensity of all processes is $\rho = 1/\pi$. The additional parameters of the Thomas process are, as used throughout the paper, $\rho_{\text{parent}} = 1/(20\pi)$, and $\sigma = 2$. We evaluated \widehat{S}_{SI} (23) on its allowed wavevectors (22), between $k_1 = 0.1$ and $k_J = 2.8$. For the other estimators, $\widehat{S}_{\text{DDT}}(t_0, \mathbf{k})$, $\widehat{S}_{\text{DDT}}(t_1, \mathbf{k})$ (32), and $\widehat{S}_{\text{DDMT}}((t_q)_{q=1}^4, \mathbf{k})$ (33), we used arbitrary wavevectors keeping the same range of the wavenumbers used for \widehat{S}_{SI} . The tapers used are t_0 (27), and the first 4 tapers $(t_q)_{q=1}^4$ of the family of sinusoidal tapers (34). As we got different approximated values of S for different wavevectors of the same wavenumber, for each wavenumber we set the estimated structure factor to the sample mean of these values.

Table 3: Paired t -tests

| Estimators | T -score | p -value | T -score | p -value | T -score | p -value |
|---|------------|---------------------|------------|---------------------|------------|--------------------|
| $\widehat{S}_{\text{DDMT}}, \widehat{S}_{\text{SI}}$ | -29.53 | 3×10^{-33} | -41.59 | 3×10^{-40} | -9.24 | 10^{-12} |
| $\widehat{S}_{\text{DDMT}}, \widehat{S}_{\text{DDT}}$ | -22.40 | 10^{-27} | -30.42 | 8×10^{-34} | -6.38 | 2×10^{-8} |
| $\widehat{S}_{\text{DDMT}}, \widehat{S}_{\text{DDT}}$ | -12.18 | 9×10^{-17} | -25.39 | 3×10^{-30} | -7.16 | 10^{-9} |
| | Ginibre | | Poisson | | Thomas | |

T -scores of the $\widehat{\text{iMSE}}$ and the associated p -values

Table 3 summarizes the results of the paired one-sided Student tests. For each point process, applying a Bonferroni correction, we can simultaneously reject at the level 0.01 the three hypotheses that there is no difference in mean between the estimated $\widehat{\text{iMSE}}$ s. This confirms our intuition that $\widehat{S}_{\text{DDMT}}((t_q)_1^4)$ yields the smallest integrated MSE among the considered variants of the scattering intensity. In particular, multitapering helps.

For information, the estimated $\widehat{\text{iMSE}}$ s are given in Table 4, in the form of a confidence interval (CI) of the $\widehat{\text{iMSE}}$ s plus or minus 3 empirical standard deviations of the mean. There is roughly a factor 4 between the $\widehat{\text{iMSE}}$ of the directly debiased multitapered estimator and each of the other three, which confirms its domination. For reference, we have also indicated the contribution of the sample integrated variance ($\widehat{\text{iVar}}$) to each $\widehat{\text{iMSE}}$. Clearly, the variance is

the biggest contributor, and the squared bias is at least one order of magnitude smaller, for all point processes.

Finally, Figure 13 shows the pointwise average of each estimator, across the 50 point process realizations. A reduction of bias at small k for $\widehat{S}_{\text{DDT}}(t_1, \mathbf{k})$ and $\widehat{S}_{\text{DDMT}}((t_q)_{q=1}^4, \mathbf{k})$ is visible for Ginibre.

Table 4: Sample integrated variance and MSE

| Estimators | $\widehat{\text{iVar}}$ | CI[$\widehat{\text{iMSE}}$] | $\widehat{\text{iVar}}$ | CI[$\widehat{\text{iMSE}}$] | $\widehat{\text{iVar}}$ | CI[$\widehat{\text{iMSE}}$] |
|---|-------------------------|-------------------------------|-------------------------|-------------------------------|-------------------------|-------------------------------|
| $\widehat{S}_{\text{SI}}(2\pi\mathbf{n}/L)$ | 0.32 | 0.32 ± 0.02 | 1.31 | 1.34 ± 0.06 | 69.51 | 70.71 ± 17.95 |
| $\widehat{S}_{\text{DDT}}(t_0)$ | 0.32 | 0.33 ± 0.03 | 1.44 | 1.47 ± 0.1 | 72.15 | 73.63 ± 26.12 |
| $\widehat{S}_{\text{DDT}}(t_1)$ | 0.34 | 0.35 ± 0.06 | 1.47 | 1.50 ± 0.14 | 79.29 | 80.51 ± 27.20 |
| $\widehat{S}_{\text{DDMT}}((t_q)_{q=1}^4)$ | 0.08 | 0.08 ± 0.007 | 0.37 | 0.38 ± 0.02 | 17.90 | 18.19 ± 4.19 |
| | Ginibre | | Poisson | | Thomas | |

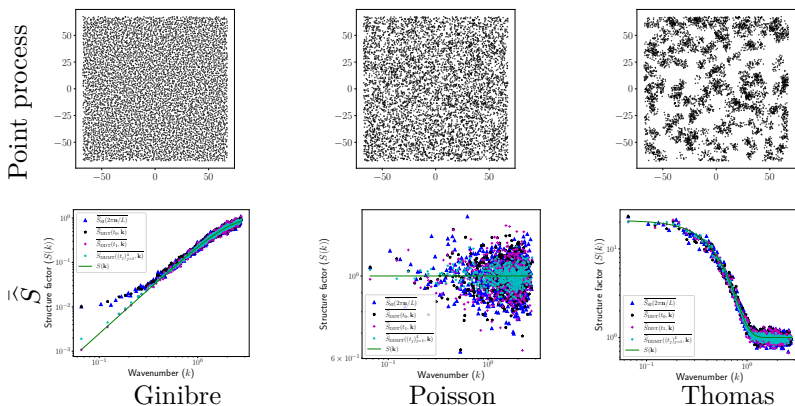


Fig. 13: Pointwise averages of the variants of the scattering intensity, numerically rotation-averaged, across 50 independent realizations of the Ginibre, Poisson, and Thomas point processes. The computation and visualization are done using `structure_factor`

6.4 Comparing estimators that assume isotropy

We now run the same comparison on \widehat{S}_{BI} (38), \widehat{S}_{HO} (43), and \widehat{S}_{HBC} (49). For this study, we have sampled 50 independent realizations of approximately 5800 points each, from the Ginibre, Poisson, and Thomas processes, with the same parameters as in Section 6.3, except that the observation window for all point processes is now a 2-dimensional ball window centered at the origin. For \widehat{S}_{HO} ,

and \widehat{S}_{HBC} we used the method `pcf.fv` to approximate the pair correlation function with maximal approximation radius $r_{\text{max}} = 30$.

We have noted in Section 5 that \widehat{S}_{HBC} is more robust to non-isotropy than \widehat{S}_{HO} , and that \widehat{S}_{BI} gave the tightest approximations in this family of estimators.

Table 5: Paired t -tests

| Estimators | T -score | p -value | T -score | p -value | T -score | p -value |
|--|------------|---------------------|------------|------------|------------|--------------------|
| \widehat{S}_{BI} vs. \widehat{S}_{HO} | -12.24 | 7×10^{-17} | -6.60 | 10^{-8} | -5.32 | 10^{-6} |
| \widehat{S}_{BI} vs. \widehat{S}_{HBC} | -25.51 | 2×10^{-30} | -5.32 | 10^{-6} | -5.16 | 2×10^{-6} |
| | Ginibre | | Poisson | | Thomas | |

T -scores of the $\widehat{\text{iMSE}}$ and the associated p -values

Table 5, summarizes the results of two one-sided paired t -tests per point process. For each point process, we can again simultaneously reject at level 0.01 the hypotheses that there is no difference between the estimates $\widehat{\text{iMSE}}$ s. This confirms the claim that Bartlett’s estimator is the most accurate near 0, among estimators that assume isotropy. For reference, Table 6 gives the same summary statistics as Table 4 did for scattering intensity variants. Bartlett’s estimator yields $\widehat{\text{iMSE}}$ s one order of magnitude smaller than both Hankel transform quadratures, for both Ginibre and Poisson, and a factor 3 for Thomas. Again, the integrated MSE is mostly variance.

Table 6: Sample integrated variance and MSE

| \widehat{S} | $\widehat{\text{iVar}}$ | $\text{CI}[\widehat{\text{iMSE}}]$ | $\widehat{\text{iVar}}$ | $\text{CI}[\widehat{\text{iMSE}}]$ | $\widehat{\text{iVar}}$ | $\text{CI}[\widehat{\text{iMSE}}]$ |
|----------------------------|-------------------------|---|-------------------------|------------------------------------|-------------------------|------------------------------------|
| \widehat{S}_{BI} | 3.9×10^{-3} | $4.0 \times 10^{-3} \pm 3 \times 10^{-4}$ | 0.057 | $0.058 \pm 9 \times 10^{-3}$ | 11.25 | 11.65 ± 4.71 |
| \widehat{S}_{HO} | 0.37 | 0.38 ± 0.09 | 2.12 | 2.14 ± 0.93 | 43.63 | 46.70 ± 18.40 |
| \widehat{S}_{HBC} | 0.03 | 0.03 ± 0.01 | 2.44 | 2.45 ± 1.33 | 57.62 | 63.02 ± 28.62 |
| | Ginibre | | Poisson | | Thomas | |

Finally, Figure 14 shows the pointwise average of each estimator, across the 50 point process realizations. The accuracy of Ogata’s quadrature at small wavenumbers is poor. The bias of the two Hankel quadrature estimators is well visible at small k for all point processes. This is likely due to poor estimation of the pair correlation function at large scales.

Summary and discussion

We surveyed estimators of the structure factor of a stationary point process, along with numerical diagnostics of hyperuniformity. We also proposed the first (asymptotic) test of hyperuniformity based on the debiasing techniques of (Rhee and Glynn, 2015). We provided an open-source Python toolbox

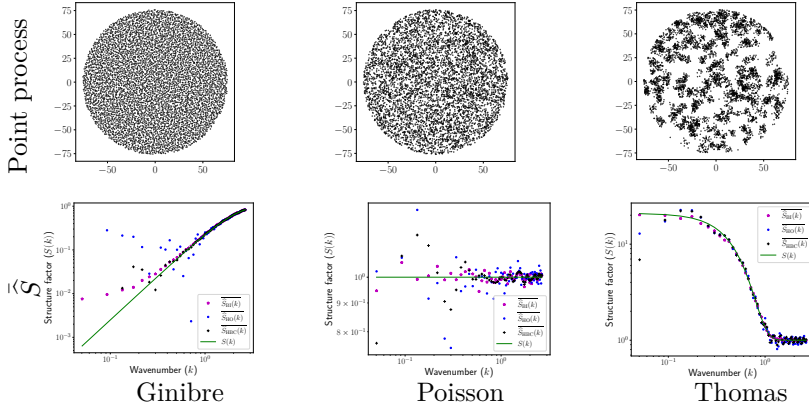


Fig. 14: Pointwise averages of the three estimators that assume isotropy, across 50 independent samples of the Ginibre, Poisson, and Thomas point processes. The computation and visualization are done using `structure_factor`

`structure_factor` containing all estimators and diagnostics and used it to benchmark known estimators. The two estimators that fared best in our benchmark are the multitapered variant of the scattering intensity and, in the case of isotropic point processes, Bartlett’s isotropic estimator. Further comparing these two estimators is a natural avenue for further work, but needs careful thinking. For starters, the two estimators are not defined on similar windows, and they do not require the same number of evaluations for a similar accuracy. Then, it is not clear how to best choose the tapers in the multitaper estimator, not even mentioning that a multitapered version of Bartlett’s estimator can also in principle be derived. On the other hand, the computational cost of Bartlett’s estimator should be lowered, e.g. by subsampling pairs of points.

Estimators based on Hankel transform quadratures, which rely on first estimating the pair correlation function g , comparatively showed poor performance. But it is still possible that estimating g first can help estimating S if, say, edge correction plays an important role. If the user only has data collected on a non-rectangular, non-ball window, we would then recommend trying the Hankel-Baddour-Chouinard estimator. For our benchmarks, though, the large cardinalities and the regular windows involved do not build upon this strong point of quadrature-based estimators. It would also be interesting to investigate edge correction, or regularization schemes for the pair correlation function, that are tailored to structure factor estimation.

On another note, since the structure factor is a Fourier transform, one might be tempted to periodize one’s sample before computing estimators. However, we do not see a clear argument for (or against) periodization yet. First, if one is using the scattering intensity applied on any of the restricted allowed wavenectors in \mathbb{A}_L^{res} , then periodizing the point process has no effect on the estimator. The case of wavenectors in \mathbb{A}_L , and of other estimators, is less straightforward. Second, adding periodic boundaries forces an arbitrary

regularity at long distances, which intuitively would impact any empirical diagnostic of hyperuniformity.

Graphical hyperuniformity diagnostics did allow us to recover known information, and conjecture a particular decay for the KLY point process. Yet, summary statistics like the H -index and the estimated power decay of the structure factor require manual choices and show large variance. More automated and low-variance estimators are desirable. Our asymptotic test is a first step in that direction.

Finally, on the point process side, we hope that our survey and software can contribute to the standardization and reproducibility of empirical investigations involving structure factors, including the study of hyperuniform point processes. For starters, it would be interesting to empirically assess how the decay of the structure factor of the KLY process depends on the initial point process that is matched with \mathbb{Z}^2 .

Acknowledgements

We thank Jean-François Coeurjolly, Michael Andreas Klatt, David Dereudre, and Simon Coste for insightful discussions along this project.

Funding

This work is supported by ERC-2019-STG-851866, ANR-20-CHIA-0002.

Declarations

Conflicts of interest/Competing interests

The authors have no conflicts of interest to declare that relate to the content of this article.

Code availability

The code is published as an open-source Python toolbox under the project name `structure-factor`. The package is licensed under the [MITlicense](#) and is available on [Github](#)⁸ and [PyPI](#)⁹.

References

- G. W. Anderson, A. Guionnet, and O. Zeitouni. *An Introduction to Random Matrices*. Cambridge University Press, Cambridge, 2009. ISBN 9780511801334. doi: 10.1017/CBO9780511801334.
- A. Baddeley, E. Rubak, and R. Turner. *Spatial Point Patterns : Methodology and Applications with R*. Chapman and Hall/CRC, nov 2015. ISBN 9780429161704. doi: 10.1201/B19708.

⁸<https://github.com/For-a-few-DPPs-more/structure-factor>

⁹<https://pypi.org/project/structure-factor/>

- N. Baddour and U. Chouinard. Theory and operational rules for the discrete Hankel transform. *Journal of the Optical Society of America A*, 32(4):611, apr 2015. ISSN 1084-7529. doi: 10.1364/JOSAA.32.000611.
- R. Bardenet and A. Hardy. Monte Carlo with determinantal point processes. *The Annals of Applied Probability*, 30(1), feb 2020. ISSN 1050-5164. doi: 10.1214/19-AAP1504.
- R. Bardenet, S. Ghosh, and M. Lin. Determinantal point processes based on orthogonal polynomials for sampling minibatches in SGD. In *Advances in Neural Information Processing Systems (NeurIPS)*, 2021.
- M. S. Bartlett. The spectral analysis of two-dimensional point processes. *Biometrika*, 51(3-4):299–311, mar 1964. ISSN 0006-3444. doi: 10.1093/biomet/51.3-4.299.
- J. Beck. Irregularities of distribution. I. *Acta Mathematica*, 159(0):1–49, 1987. ISSN 0001-5962. doi: 10.1007/BF02392553.
- A. Belhadji, R. Bardenet, and P. Chainais. Kernel quadrature with DPPs. In *Advances in Neural Information Processing Systems (NeurIPS)*, volume 32, pages 12927–12937, 2019.
- A. Belhadji, R. Bardenet, and P. Chainais. Kernel interpolation with continuous volume sampling. In H. D. III and A. Singh, editors, *International Conference on Machine Learning (ICML)*, volume 119 of *Proceedings of Machine Learning Research*, pages 725–735. PMLR, 2020a.
- A. Belhadji, R. Bardenet, and P. Chainais. A determinantal point process for column subset selection. *Journal of Machine Learning Research*, 21(197): 1–62, 2020b.
- C. A. N. Biscio and R. Waagepetersen. A general central limit theorem and a subsampling variance estimator for α -mixing point processes. *Scandinavian Journal of Statistics*, 46(4):1168–1190, dec 2019. ISSN 0303-6898. doi: 10.1111/sjos.12389.
- J. Boursier. Optimal local laws and CLT for 1D long-range Riesz gases. *ArXiv e-prints*, Dec 2021. doi: 10.48550/arXiv.2112.05881.
- S. N. Chiu, D. Stoyan, W. Kendall, and J. Mecke. *Stochastic Geometry and its Applications*. Wiley Series in Probability and Statistics. Wiley, aug 2013. ISBN 9780470664810. doi: 10.1002/9781118658222.
- S. Coste. Order, fluctuations, rigidities. 2021.

- P. J. Diggle, D. J. Gates, and A. Stibbard. A nonparametric estimator for pairwise-interaction point processes. *Biometrika*, 74(4):763–770, dec 1987. ISSN 0006-3444. doi: 10.1093/BIOMET/74.4.763.
- M. Guizar-Sicairos and J. C. Gutiérrez-Vega. Computation of quasi-discrete Hankel transforms of integer order for propagating optical wave fields. *Journal of the Optical Society of America A*, 21(1):53, jan 2004. ISSN 1084-7529. doi: 10.1364/JOSAA.21.000053.
- J. B. Hough, M. Krishnapur, Y. Peres, and B. Virág. *Zeros of Gaussian analytic functions and determinantal point processes*, volume 51. American Mathematical Society, 2009. ISBN 978-0-8218-4373-4.
- M. A. Klatt, J. Lovrić, D. Chen, S. C. Kapfer, F. M. Schaller, P. W. A. Schönhöfer, B. S. Gardiner, A.-S. Smith, G. E. Schröder-Turk, and S. Torquato. Universal hidden order in amorphous cellular geometries. *Nature Communications*, 10(1):811, dec 2019. ISSN 2041-1723. doi: 10.1038/s41467-019-08360-5.
- M. A. Klatt, G. Last, and D. Yogeshwaran. Hyperuniform and rigid stable matchings. *Random Structures & Algorithms*, 57(2):439–473, sep 2020. ISSN 1042-9832. doi: 10.1002/rsa.20923.
- L. J. Landau. Bessel Functions: Monotonicity and Bounds. *Journal of the London Mathematical Society*, 61(1):197–215, feb 2000. ISSN 00246107. doi: 10.1112/S0024610799008352.
- S. Murray and F. Poulin. hankel: A Python library for performing simple and accurate Hankel transformations. *Journal of Open Source Software*, 4(37):1397, may 2019. ISSN 2475-9066. doi: 10.21105/joss.01397.
- H. Ogata. A numerical integration formula based on the Bessel functions. *Publications of the Research Institute for Mathematical Sciences*, 41(4):949–970, 2005. ISSN 0034-5318. doi: 10.2977/prims/1145474602.
- B. Osgood. *Lecture Notes for EE 261 the Fourier Transform and Its Applications*. CreateSpace Independent Publishing Platform, 2014. ISBN 9781505614497.
- D. B. Percival and A. T. Walden. *Spectral Analysis for Univariate Time Series*, volume 51. Cambridge University Press, mar 2020. ISBN 9781139235723. doi: 10.1017/9781139235723.
- T. A. Rajala, S. C. Olhede, and D. J. Murrell. Spectral estimation for spatial point patterns. *ArXiv e-prints*, sep 2020. doi: 10.48550/arxiv.2009.01474.

C.-h. Rhee and P. W. Glynn. Unbiased estimation with square root convergence for SDE models. *Operations Research*, 63(5):1026–1043, 2015. Publisher: INFORMS.

K. Riedel and A. Sidorenko. Minimum bias multiple taper spectral estimation. *IEEE Transactions on Signal Processing*, 43(1):188–195, mar 1995. ISSN 1053587X. doi: 10.1109/78.365298.

D. J. Thomson. Spectrum estimation and harmonic analysis. *Proceedings of the IEEE*, 70(9):1055–1096, 1982. ISSN 0018-9219. doi: 10.1109/PROC.1982.12433.

S. Torquato. Hyperuniform states of matter. *Physics Reports*, 745:1–95, jun 2018. ISSN 03701573. doi: 10.1016/j.physrep.2018.03.001.

A Proof of Proposition 3

Proof Let $M \in L^p$ with $p > 0$. We first prove that $Z_m \rightarrow Z$ in L^p . As we have $Z_m \rightarrow Z$ a.s., it is enough to show that Z_m is uniformly bounded in L^p . For a realization M' of M we have,

$$|Z_m| \leq \sum_{j=1}^{m \wedge M'} \frac{|Y_j - Y_{j-1}|}{\mathbb{P}(M \geq j)} \leq \frac{M'}{\mathbb{P}(M \geq M')}.$$

By assumption $M \in L^p$ so Z_m is uniformly bounded in L^p . This proves the first part of the proposition.

Before proving the additional two points, note that, since S is continuous,

$$\mathbb{E}[\widehat{S}_m(\mathbf{k}_m^{\min})] \xrightarrow{m \rightarrow \infty} S(\mathbf{0}). \tag{56}$$

Now, let us prove the first point of the proposition. Assume that $M \in L^1$ and \mathcal{X} is hyperuniform, so that $S(\mathbf{0}) = 0$. Since \widehat{S}_m is nonnegative, Equation (56) yields

$$\widehat{S}_m(\mathbf{k}_m^{\min}) \xrightarrow{m \rightarrow \infty} 0.$$

Moreover, letting $f : x \mapsto 1 \wedge x$, $|f(x)| \leq x$ on \mathbb{R}^+ , so that

$$\mathbb{E}[|f(\widehat{S}_m(\mathbf{k}_m^{\min}))|] \leq \mathbb{E}[\widehat{S}_m(\mathbf{k}_m^{\min})] \rightarrow 0,$$

and

$$Y_m = f(\widehat{S}_m(\mathbf{k}_m^{\min})) \xrightarrow{m \rightarrow \infty} 0. \tag{57}$$

Since $\mathbb{E}[Y_m] = \mathbb{E}[Z_m]$ and Z_m converges in L^1 to Z , by unicity of the limit, we have $\mathbb{E}[Z] = 0$.

It remains to show the last point of the proposition. Assume again that $M \in L^1$, but that \mathcal{X} is not hyperuniform, so that $S(\mathbf{0}) > 0$. Reasoning by contradiction, assume that $\mathbb{E}[Z] = 0$. As $\mathbb{E}[Y_m] = \mathbb{E}[Z_m]$ and Z_m converges in L^1 to Z , we get

$$\mathbb{E}[\widehat{S}_m(k_m^{\min}) \mathbf{1}_{\{\widehat{S}_m(k_m^{\min}) < 1\}}] \xrightarrow{m \rightarrow \infty} 0, \tag{58}$$

and

$$\mathbb{E}[\mathbf{1}_{\{\widehat{S}_m(k_m^{\min}) \geq 1\}}] \xrightarrow{m \rightarrow \infty} 0. \tag{59}$$

Meanwhile,

$$\mathbb{E}[\widehat{S}_m(k_m^{\min})] \xrightarrow{m \rightarrow \infty} S(\mathbf{0}) > 0.$$

Using Equation (58), we get

$$\mathbb{E}[\widehat{S}_m(k_m^{\min}) \mathbb{1}_{\{\widehat{S}_m(k_m^{\min}) \geq 1\}}] \xrightarrow{m \rightarrow \infty} S(\mathbf{0}) > 0. \quad (60)$$

Finally, Cauchy-Schwarz, together with Condition (53) and Equation (59) yield

$$\begin{aligned} & \mathbb{E}[\widehat{S}_m(k_m^{\min}) \mathbb{1}_{\{\widehat{S}_m(k_m^{\min}) \geq 1\}}] \leq \\ & \mathbb{E}^{1/2}[\widehat{S}_m^2(k_m^{\min})] \times \mathbb{E}^{1/2}[\mathbb{1}_{\{\widehat{S}_m(k_m^{\min}) \geq 1\}}] \rightarrow 0, \end{aligned}$$

which contradicts Equation (60) and ends the proof. \square

B Validity of Assumption (53)

In what follows, we show that Assumption (53) is satisfied for a homogeneous Poisson point process \mathcal{X} of intensity ρ , $\widehat{S} = \widehat{S}_{\text{SI}}$, and W_m are increasing rectangular windows.

Let $N_m = |\mathcal{X} \cap W_m|$. Then,

$$\begin{aligned} \rho^2 |W_m|^2 \mathbb{E}[\widehat{S}_m^2(\mathbf{k})] &= \mathbb{E} \left(\left| \sum_{\mathbf{x} \in \mathcal{X} \cap W_m} e^{-i\langle \mathbf{k}, \mathbf{x} \rangle} \right|^2 \right)^2 \\ &= \mathbb{E} \left[N_m^2 + \left(\sum_{\substack{\mathbf{x} \neq \mathbf{y} \\ \mathbf{x}, \mathbf{y} \in \mathcal{X} \cap W_m}} e^{-i\langle \mathbf{k}, \mathbf{x} - \mathbf{y} \rangle} \right)^2 + 2N_m \sum_{\substack{\mathbf{x} \neq \mathbf{y} \\ \mathbf{x}, \mathbf{y} \in \mathcal{X} \cap W_m}} e^{-i\langle \mathbf{k}, \mathbf{x} - \mathbf{y} \rangle} \right] \\ &= \mathbb{E} \left[2N_m^2 - N_m + \sum_{\substack{\mathbf{x} \neq \mathbf{y} \\ \mathbf{x}, \mathbf{y} \in \mathcal{X} \cap W_m}} 2N_m e^{-i\langle \mathbf{k}, \mathbf{x} - \mathbf{y} \rangle} + e^{-i2\langle \mathbf{k}, \mathbf{x} - \mathbf{y} \rangle} \right. \\ & \quad + \sum_{\substack{\mathbf{x} \neq \mathbf{y} \neq \mathbf{z} \\ \mathbf{x}, \mathbf{y}, \mathbf{z} \in \mathcal{X} \cap W_m}} 2e^{-i\langle \mathbf{k}, \mathbf{x} - \mathbf{y} \rangle} + e^{-i\langle \mathbf{k}, 2\mathbf{x} - \mathbf{y} - \mathbf{z} \rangle} + e^{i\langle \mathbf{k}, 2\mathbf{x} - \mathbf{y} - \mathbf{z} \rangle} \\ & \quad \left. + \sum_{\substack{\mathbf{x} \neq \mathbf{y} \neq \mathbf{z} \neq \mathbf{t} \\ \mathbf{x}, \mathbf{y}, \mathbf{z}, \mathbf{t} \in \mathcal{X} \cap W_m}} e^{-i\langle \mathbf{k}, \mathbf{x} - \mathbf{y} + \mathbf{z} - \mathbf{t} \rangle} \right] \\ &= \mathbb{E} \left[2N_m^2 - N_m + \sum_{\substack{\mathbf{x} \neq \mathbf{y} \\ \mathbf{x}, \mathbf{y} \in \mathcal{X} \cap W_m}} 4e^{-i\langle \mathbf{k}, \mathbf{x} - \mathbf{y} \rangle} + e^{-i2\langle \mathbf{k}, \mathbf{x} - \mathbf{y} \rangle} \right. \\ & \quad + \sum_{\substack{\mathbf{x} \neq \mathbf{y} \neq \mathbf{z} \\ \mathbf{x}, \mathbf{y}, \mathbf{z} \in \mathcal{X} \cap W_m}} 4e^{-i\langle \mathbf{k}, \mathbf{x} - \mathbf{y} \rangle} + e^{-i\langle \mathbf{k}, 2\mathbf{x} - \mathbf{y} - \mathbf{z} \rangle} + e^{i\langle \mathbf{k}, 2\mathbf{x} - \mathbf{y} - \mathbf{z} \rangle} \\ & \quad \left. + \sum_{\substack{\mathbf{x} \neq \mathbf{y} \neq \mathbf{z} \neq \mathbf{t} \\ \mathbf{x}, \mathbf{y}, \mathbf{z}, \mathbf{t} \in \mathcal{X} \cap W_m}} e^{-i\langle \mathbf{k}, \mathbf{x} - \mathbf{y} + \mathbf{z} - \mathbf{t} \rangle} \right] \\ &= \mathbb{E}[2N_m^2 - N_m] + \int_{W_m \times W_m} \left(4e^{-i\langle \mathbf{k}, \mathbf{x} - \mathbf{y} \rangle} + e^{-i2\langle \mathbf{k}, \mathbf{x} - \mathbf{y} \rangle} \right) \rho^2 dx dy \end{aligned}$$

$$\begin{aligned}
& + \int_{W_m \times W_m \times W_m} \left(4e^{-i\langle \mathbf{k}, \mathbf{x} - \mathbf{y} \rangle} + e^{-i\langle \mathbf{k}, 2\mathbf{x} - \mathbf{y} - \mathbf{z} \rangle} \right. \\
& \qquad \qquad \qquad \left. + e^{i\langle \mathbf{k}, 2\mathbf{x} - \mathbf{y} - \mathbf{z} \rangle} \right) \rho^3 d\mathbf{x}d\mathbf{y}d\mathbf{z} \\
& + \int_{W_m \times W_m \times W_m \times W_m} e^{-i\langle \mathbf{k}, \mathbf{x} - \mathbf{y} + \mathbf{z} - \mathbf{t} \rangle} \rho^4 d\mathbf{x}d\mathbf{y}d\mathbf{z}d\mathbf{t}.
\end{aligned}$$

The last line was obtained using the definition of the n -th product density $\rho^{(n)}$ and that for any $n \geq 1$, $\rho^{(n)}$ of \mathcal{X} simplifies to ρ^n . It is a well-known property of homogeneous Poisson point processes (Chiu et al., 2013, Section 2.3.3). Now, using the parity of $\mathbf{1}_{W_m}$ and that N_m is a Poisson r.v., we get

$$\begin{aligned}
\mathbb{E}[\widehat{S}_m^2(\mathbf{k}_m^{\min})] &= \frac{1}{(\rho|W_m|)^2} \left[\rho|W_m| + 2(\rho|W_m|)^2 + \rho^4 \mathcal{F}^4(\mathbf{1}_{W_m})(\mathbf{k}_m^{\min}) \right. \\
& \quad + \rho^2 \left(4\mathcal{F}^2(\mathbf{1}_{W_m})(\mathbf{k}_m^{\min}) + \mathcal{F}^2(\mathbf{1}_{W_m})(2\mathbf{k}_m^{\min}) \right) \\
& \quad \left. + \rho^3 \left(4|W_m| \mathcal{F}^2(\mathbf{1}_{W_m})(\mathbf{k}_m^{\min}) + 2\mathcal{F}(\mathbf{1}_{W_m})(2\mathbf{k}_m^{\min}) \mathcal{F}^2(\mathbf{1}_{W_m})(\mathbf{k}_m^{\min}) \right) \right].
\end{aligned} \tag{61}$$

Upon noting that $\mathbf{k}_m^{\min} = (\frac{2\pi}{L_1}, \dots, \frac{2\pi}{L_d})$ and

$$\mathcal{F}(\mathbf{1}_{W_m})(\mathbf{k}) = \prod_{j=1}^d \frac{\sin(k_j L_j / 2)}{k_j / 2}.$$

Equation (61) simplifies to

$$\mathbb{E}[\widehat{S}_m^2(\mathbf{k}_m^{\min})] = \frac{1}{\rho|W_m|} + 2.$$

Thus Assumption (53) holds.